Article

Cell Reports

A comprehensive atlas of perineuronal net distribution and colocalization with parvalbumin in the adult mouse brain

Graphical abstract

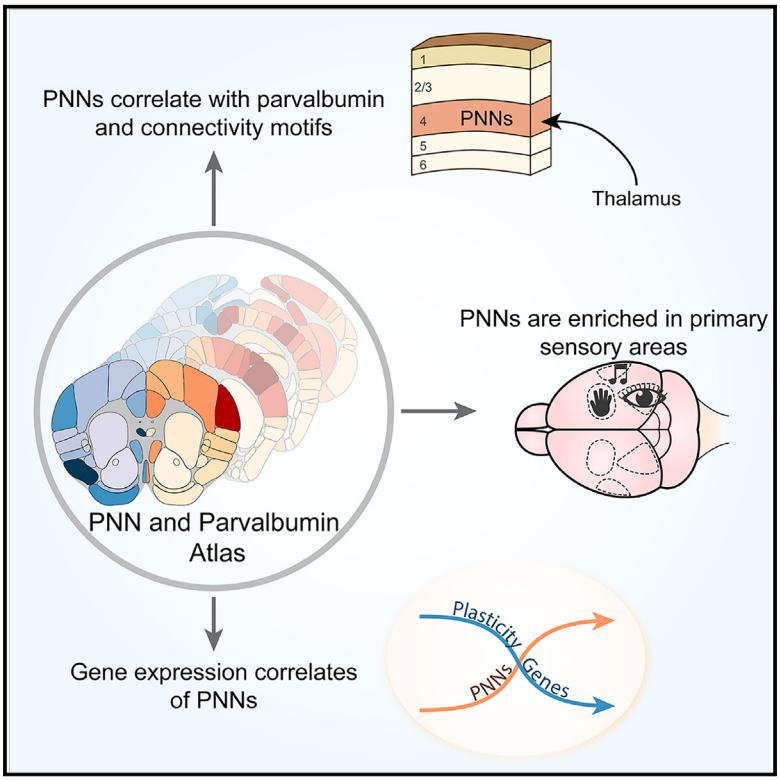

Authors

Leonardo Lupori, Valentino Totaro, Sara Cornuti, ..., Claudio Gennaro, Paola Tognini, Tommaso Pizzorusso

Correspondence

tommaso.pizzorusso@sns.it

In brief

Lupori et al. report an atlas of perineuronal nets (PNNs) and parvalbumin (PV) cells in the adult mouse brain. Data analysis shows that PV expression and connectivity are determinants of PNN expression. Gene expression analysis shows PNN-anticorrelated transcripts enriched in synaptic plasticity genes, supporting PNNs' role in circuit stability.

Highlights

- A mouse brain atlas of perineuronal nets (PNNs) and parvalbumin (PV)-positive cells
- PV expression is a good predictor of PNN aggregation
- PNNs are enriched in layer 4 of primary sensory cortices in correlation with thalamic input
- PNN-anticorrelated transcripts are enriched in synaptic plasticity genes

Lupori et al., 2023, Cell Reports *42*, 112788
July 25, 2023
https://doi.org/10.1016/j.celrep.2023.112788

CellPress

Cell Reports

CellPress
OPEN ACCESS

Article

A comprehensive atlas of perineuronal net distribution and colocalization with parvalbumin in the adult mouse brain

Leonardo Lupori,[1,5] Valentino Totaro,[1,5] Sara Cornuti,[1] Luca Ciampi,[2] Fabio Carrara,[2] Edda Grilli,[4] Aurelia Viglione,[1] Francesca Tozzi,[1] Elena Putignano,[3] Raffaele Mazziotti,[3] Giuseppe Amato,[2] Claudio Gennaro,[2] Paola Tognini,[4] and Tommaso Pizzorusso[1,3,6,*]

[1]BIO@SNS Lab, Scuola Normale Superiore, 56126 Pisa, Italy
[2]Institute of Information Science and Technologies (ISTI-CNR), 56124 Pisa, Italy
[3]Institute of Neuroscience (IN-CNR), 56124 Pisa, Italy
[4]Department of Translational Research and New Technologies in Medicine and Surgery, University of Pisa, 56126 Pisa, Italy
[5]These authors contributed equally
[6]Lead contact
*Correspondence: tommaso.pizzorusso@sns.it
https://doi.org/10.1016/j.celrep.2023.112788

SUMMARY

Perineuronal nets (PNNs) surround specific neurons in the brain and are involved in various forms of plasticity and clinical conditions. However, our understanding of the PNN role in these phenomena is limited by the lack of highly quantitative maps of PNN distribution and association with specific cell types. Here, we present a comprehensive atlas of *Wisteria floribunda* agglutinin (WFA)-positive PNNs and colocalization with parvalbumin (PV) cells for over 600 regions of the adult mouse brain. Data analysis shows that PV expression is a good predictor of PNN aggregation. In the cortex, PNNs are dramatically enriched in layer 4 of all primary sensory areas in correlation with thalamocortical input density, and their distribution mirrors intracortical connectivity patterns. Gene expression analysis identifies many PNN-correlated genes. Strikingly, PNN-anticorrelated transcripts are enriched in synaptic plasticity genes, generalizing PNNs' role as circuit stability factors.

INTRODUCTION

PNNs are specialized reticular structures of the extracellular matrix (ECM) that ensheath neurons in the entire mouse and human brain.[1–4] These structures aggregate progressively during postnatal development, in parallel with the closure of critical periods for developmental plasticity.[5–9] Although their precise composition may vary between different brain regions, PNNs are known to share four essential molecular constituents: hyaluronic acid, glycosylated proteins called chondroitin sulfate proteoglycans (CSPGs), link proteins such as hyaluronan and proteoglycan link protein 1 (Hapln1), and Tenascin-R.[10–12] The N-acetylgalactosamine moiety of chondroitin sulfate glycosaminoglycans is the binding target of the lectin *Wisteria floribunda* agglutinin (WFA), the most widely used marker to visualize PNNs in histological analyses.[13,14]

The precise contribution of PNNs in regulating brain function is a strongly active area of research. Many roles have been proposed, but a key overarching theme is that PNNs tightly control the plasticity and stability of neuronal circuits.[15,16] This function has been studied throughout many cortical and subcortical regions of the brain. For example, PNNs are known to control ocular dominance plasticity in the visual cortex,[7,10,17–19] fear memory extinction in the amygdala,[20,21] spatial representation stability of grid cells in the entorhinal cortex,[22] associative motor learning in the cerebellum,[23] and social memory in the hippocampus.[24,25] Enzymatic digestion of PNNs has been shown to promote plasticity and improve recovery after damage to the central nervous system.[26] Additionally, PNNs are thought to stabilize neuronal circuitry by protecting fast-spiking neurons against oxidative stress,[27] a risk factor for psychiatric diseases. Abnormalities in PNNs that make PV cells more susceptible to oxidative damage have been reported in patients with schizophrenia.[28]

Despite these general features, PNNs also show a remarkable degree of variability between different brain regions both in terms of structure and function.[29] In the isocortex, several studies showed that PNNs primarily surround fast-spiking GABAergic PV interneurons. However, in the hippocampal CA2 and in other areas, they also ensheath excitatory pyramidal neurons, suggesting a different biological function in these regions.[30] At the functional level, the enzymatic removal of PNNs can have different effects.[31] For example, it enhances long-term depression (LTD) in the perirhinal cortex,[32] while it impairs both early-phase long-term potentiation (LTP) and LTD in the hippocampus.[33] The lack of understanding of the principles of PNN organization throughout the brain hinders our comprehension of their functional role and possible

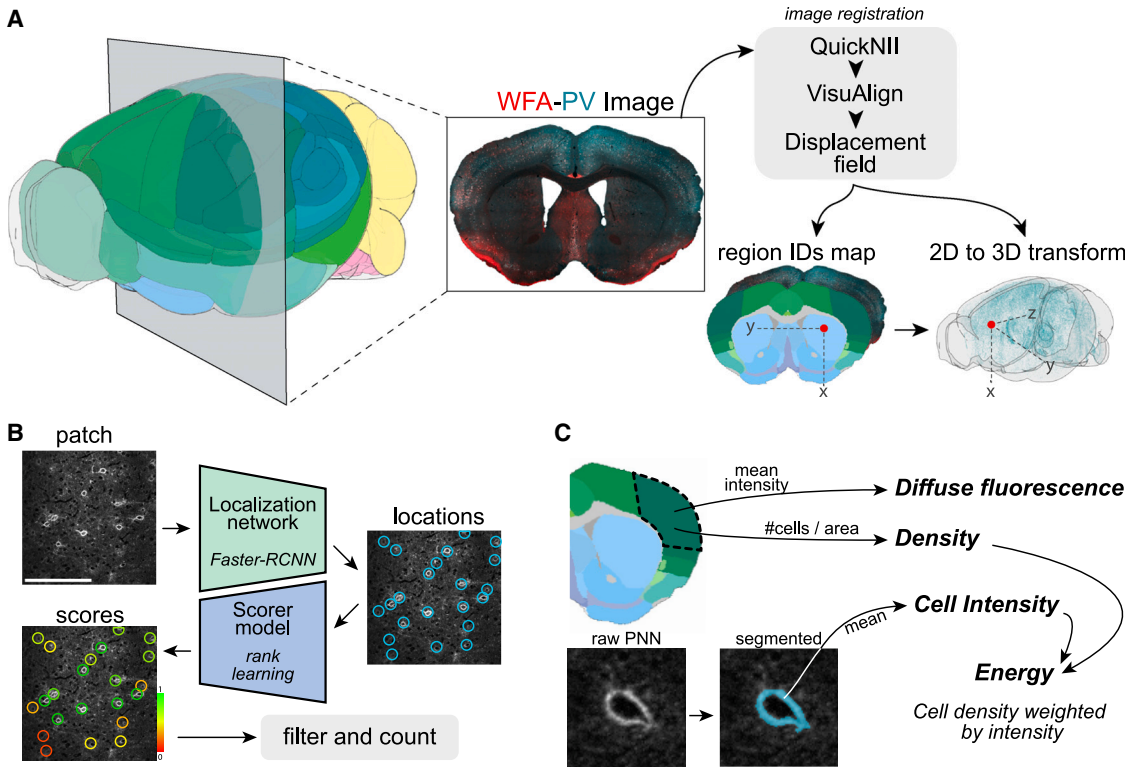

Figure 1. Image registration and analysis pipeline

(A) Schematic of the pipeline for slice registration to the Allen Institute CCFv3-2017 reference volume.

(B) Schematic of the strategy for cell counting. Two different modules were used, a larger convolutional neural network for localization and a smaller one for scoring. Scale bar, 200 μm.

(C) Diagram showing a graphical explanation of the four metrics used to quantify PNN and PV staining.

therapeutic implications. Furthermore, the link between PNNs and PV cells has not been systematically studied across brain areas.

Here, we present a systematic brain-wide analysis of PNNs and PV neurons in the mouse brain. We provide multiple quantitative measurements for PNNs, PV cells, and their interaction for more than 600 different brain areas. We also release two deep-learning models, pre-trained on a dataset of approximately 0.8 million manually annotated PNNs and PV cells, for their automatic detection. Finally, we demonstrate that, thanks to our dataset, it is possible to detect connectivity and gene expression patterns that correlate with the presence of PNNs. We believe that these resources will have a significant impact on facilitating research on PNNs.

RESULTS

PNN and PV cell quantification in the mouse brain

We performed immuno-/lectin histochemistry on serially collected whole-brain coronal slices of seven adult mice, staining sections with both WFA and an anti-PV antibody (Figure 1A). We then acquired fluorescence images and registered them to the Allen Institute CCFv3-2017.

To automatically detect the (x,y) coordinates of PNNs and PV cells, we trained two deep convolutional neural networks with a dataset comprising roughly 0.67 million manually annotated PNNs and 0.16 million PV cells (Figure 1B). To deal with annotation biases inherent to manual cell count, we implemented a second stage whereby we assigned a confidence score to each object detected by the two deep neural networks.[34] This scorer module consisted of other two models trained on two smaller datasets (4,727 PNNs and 5,738 PV cells) labeled by seven independent expert raters. The aim was to produce scores for each putative object that maximally correlate with the raters' agreement.

In our multi-rater dataset, the average agreement (Jaccard index) between pairs of expert raters was 64% for PNNs and 72% for PV cells, demonstrating relevant individual differences in counting strategies (Figure S1A). Our scoring models produced detection scores that strongly correlated with the number of raters that detected each object (Figures S1B and S1C). Overall, when tested on objects located by at least three raters, our models proved to be reliable in the detection of PNNs and PV cells (see section "deep-learning models for cell counting" in STAR Methods). We release the pre-trained four models used in this study to allow performing predictions on new images or to fine-tune them based on different experimental setups.

To quantify PV and WFA staining, we defined a set of metrics describing either "general" or "cellular" aspects of the staining signal (Figure 1C). To quantify general staining intensity in a

region, we defined "diffuse fluorescence" as the average pixel intensity value in that region. This measure includes the signal coming from both interstitial CSPGs diffusely present in the ECM and from CSPGs aggregated in PNNs. To quantify cellular aspects (either single PV cells or cell-ensheathing PNNs), we first defined "density" corresponding to the number of objects per unit of surface area. We then measured the intensity of each individual PNN and PV cell by averaging the values of the pixels belonging to the object, segmented from a small (80 × 80 pixels) patch centered on its (x,y) coordinates. Based on this measurement, we defined "cell intensity," expressing the average staining intensity of individual PNNs or PV cells in a region. PNN intensity has been found to be co-modulated with circuit plasticity during postnatal development,[35] after environmental enrichment,[36] and after manipulation of the levels of microRNA-29.[37]

Finally, we reasoned that the functional relevance of PNNs or PV cells might be better represented by a single metric that integrates both the density and the intensity of cells. We thus defined "energy" as the density weighted by intensity, a metric analogous to the one used by the Allen Institute gene expression dataset[38] (Figure 1C, see section "staining metrics definitions" in STAR Methods for details). Diffuse fluorescence and energy were normalized within each mouse by dividing them by their respective value calculated on the entire brain. As a result, a value of 1 equals the brain's average and, importantly, the two metrics have the same scale. In the rest of the paper, we will use the metrics diffuse fluorescence and energy respectively as a general and cellular measurement.

Distribution of PNNs across the mouse brain

To describe the distribution of PNNs in the entire brain, we first aggregated data in 12 major brain subdivisions (Figure 2A). These regions had highly different values of WFA diffuse fluorescence with particular enrichment in the cortex and in posterior areas of the brain (Figures 2A and 2B; see Table S1). We then analyzed PNN energy, representing PNNs in a region. Using this metric, the differences between the studied areas were more pronounced than those observed in measurements of diffuse fluorescence (Figures 2A and 2B).

We then grouped data in a set of 316 mid-ontology brain regions (Figures 2B and S2, see Table S3 for area acronyms). The profile of both metrics was consistent across individual mice and it showed that individual brain areas have remarkably diverse values for both diffuse fluorescence and PNN energy even within the same major subdivision (Figures 2C and 2F). To visualize the results at this granularity, we plotted the average of both metrics across mice in a series of brain heatmaps coronally sliced at 12 anteroposterior locations (Figure 2C).

Intriguingly, both the diffuse and cellular measurements of PNNs often varied together. However, some areas showed striking differences between the two metrics (Figure 2C). Thus, we asked whether the presence of PNNs in an area is always associated with a high level of diffuse WFA staining in all brain regions. To answer this question, we plotted WFA diffuse fluorescence versus PNN energy for all the major brain subdivisions (Figure 2D). Isocortex, midbrain, pons, and medulla were skewed toward the top-left side of the plot, indicating that they are characterized by strong individual aggregated PNNs, but relatively weak diffuse WFA signal. Conversely, all the other brain subdivisions showed the opposite effect. Notably, for the olfactory areas, we measured the highest difference between the two metrics, with a strong level of diffuse fluorescence but almost absent aggregated PNNs. This pattern was not due to background staining because negative control sections in which WFA was omitted (n = 3 mice from a separate cohort) showed that the contribution of background fluorescence was negligible (Figures S1D and S1E). We then split the 12 subdivisions into mid-ontology regions and explored the relationship between the two metrics within each group of brain areas (Figure 2E). We found that WFA diffuse fluorescence and PNN energy were significantly correlated in all subdivisions except for olfactory areas and the cortical subplate, although the strength of such correlation was not uniform. Striatum had the lowest correlation (r_s = 0.62), while midbrain and pallidum showed the highest correlation between metrics (r_s = 0.96 and 0.95 respectively). These results demonstrate that PNN abundance is not defined at the macrostructure level and that diffuse WFA staining is not necessarily correlated with numerous and strongly labeled PNNs.

Overall, these data represent a systematic and highly quantitative description of the distribution of WFA-positive PNNs in the entire mouse brain. Raw measurements for individual mice at three levels of anatomical granularity are available in Data S1.

Brain-wide analysis of the colocalization between PNNs and PV cells

In the same brain slices used for PNN analysis, we also quantified PV-positive neurons (Figure 3A) using the same procedures and metrics used for PNNs (Figure S3 and Table S2; Data S2). PV cell distribution has been analyzed in previous studies and our results show an overall analogous profile despite methodological differences.[39,40] To explore the relationship between PNNs and PV cells in the entire brain, we quantified their colocalization as the percentage of PNNs containing a PV cell (PV^+ PNNs) or as the percentage of PV cells that are surrounded by a PNN (WFA^+ PV cells). On average, in the entire brain, 59.1% ± 1.0% of PNNs were located around a PV cell, while about one-third of all PV cells in the brain (30.4% ± 1.4%) were surrounded by a PNN. After splitting the data into 12 brain subdivisions, we found that the relationship between PNNs and PV cells was highly heterogeneous (Figure 3B). In the isocortex, PNNs surrounded PV cells in more than 70% of the cases, reaching, for example, 81.1% ± 0.7% in the retrosplenial cortex (RSPv), 80.8% ± 0.4% in layer 4 of the primary visual cortex (VISp4), and 77.4% ± 0.3% in the anterior cingulate area (ACAv). In all the other major subdivisions, at least one-third of the PNNs surrounded PV cells.

Conversely, analyzing the percentage of PV cells surrounded by a PNN, we observed that in most brain areas, only between 20% and 30% of the PV cells are enwrapped by a PNN. A different pattern was present in the isocortex, hippocampal formation, and striatum, where colocalization was much higher (between 40% and 50% of PV cells, reaching for example 71.9 ± 0.4% in VISp4), while in the cerebellum only few PV-positive cells had a PNN, likely due to the high number of Purkinje cells in the cerebellar cortex that lack PNNs.[41,42] As before, we

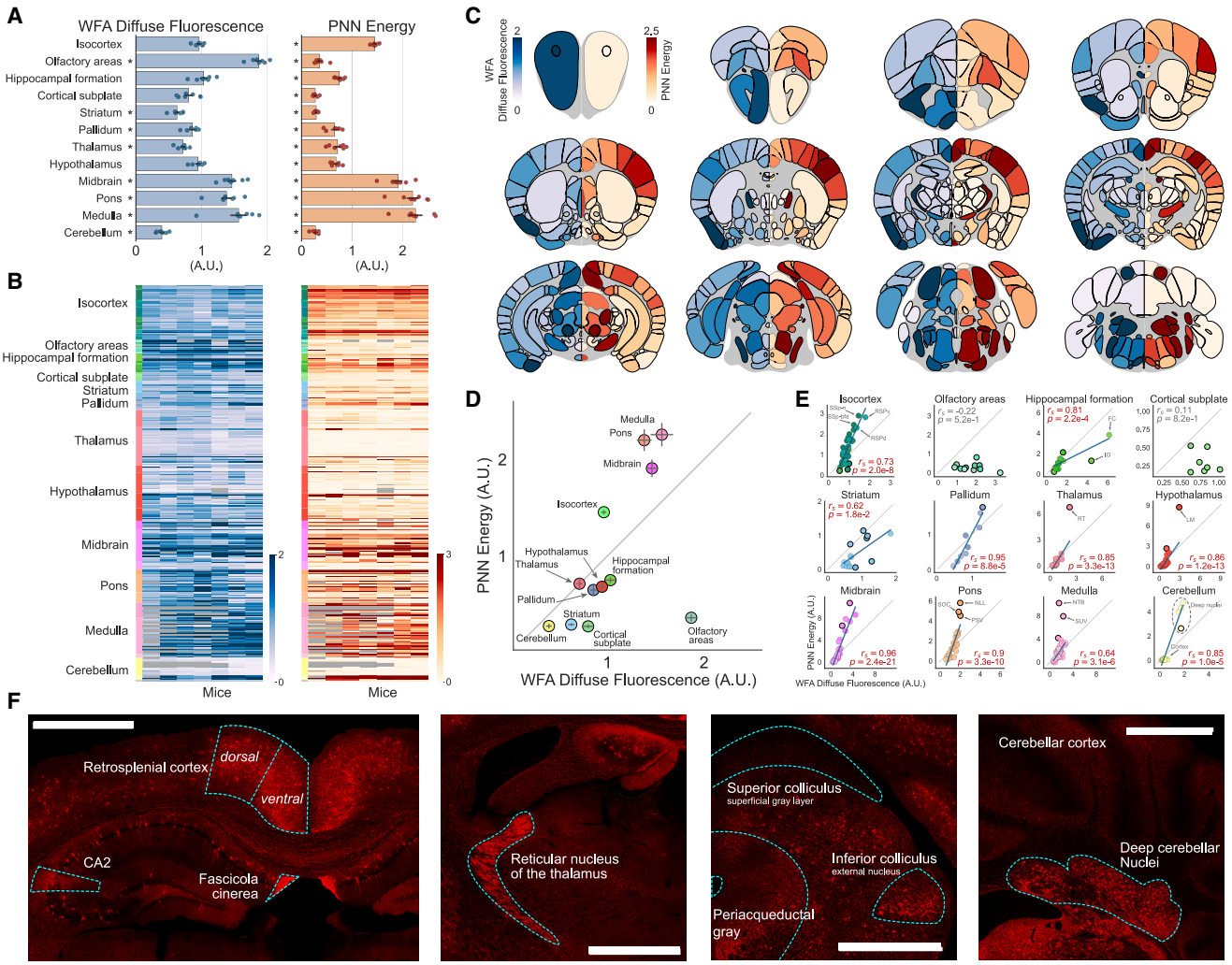

Figure 2. Distribution of WFA-positive PNNs throughout the mouse brain

(A) Diffuse fluorescence and PNN energy for 12 major brain subdivisions. Asterisks indicate subdivisions significantly different from the brain average (Table S1).

(B) Heatmaps showing staining metrics for mid-ontology brain regions in individual mice. Grayed-out cells represent regions where data are not available.

(C) Heatmaps showing coronal sections of the brain sliced at different anteroposterior locations. Left hemisphere (blue colormap), average diffuse WFA fluorescence; right hemisphere (red colormap), average PNN energy.

(D) PNN energy versus WFA diffuse fluorescence for each of the 12 major brain subdivisions.

(E) Same as in (D) but data are split in each region of the 12 major brain subdivisions.

(F) Representative WFA staining in a selection of brain areas. Scale bar, 1 mm. Error bars in (A) and (D) represent SEM across mice. Dots in (A) represent mice, in (D) and (E) represent brain regions. In (E), text insets indicate the Spearman correlation coefficient (r_s) and the corresponding p value, the gray line indicates the X-Y bisector, and, for significant correlations (highlighted in red), the blue line shows the best linear fit.

also aggregated data in mid-ontology brain regions and measured colocalization metrics at finer granularity (Figures 3C and S4). Colocalization data are available in Data S3.

We next asked whether PNN and PV staining were correlated across brain regions. We found that, throughout all areas of the brain, WFA and PV staining metrics were significantly correlated (Figures 3D and 3F, r_s = 0.38 for WFA diffuse vs. PV energy, r_s = 0.58 for PNN energy vs. PV energy). When performing the same analysis at a finer resolution, however, only a subset of brain subdivisions (isocortex, thalamus, hypothalamus, midbrain, and medulla) showed a high degree of correlation between WFA diffuse staining and PV (Figures 3E and 3G). When we compared PNN and PV energy, correlation coefficients increased in some areas, with isocortex showing the most striking trend (Figure 3G). Here, PV energy alone was highly predictive of the presence of PNNs (r_s = 0.91). Few specific areas deviated from the expected correlation pattern (for example, the arcuate nucleus and the lateral mammillary nucleus in the hypothalamus).

Our data also revealed that a substantial percentage of PNNs do not enwrap PV-positive cells (PV$^-$ PNN). Thus, we explored the energy distribution of PV$^-$ PNNs in the brain (Figure S5). The data indicate that they are present at particularly high levels in the pons, medulla, and midbrain.

CellPress
OPEN ACCESS

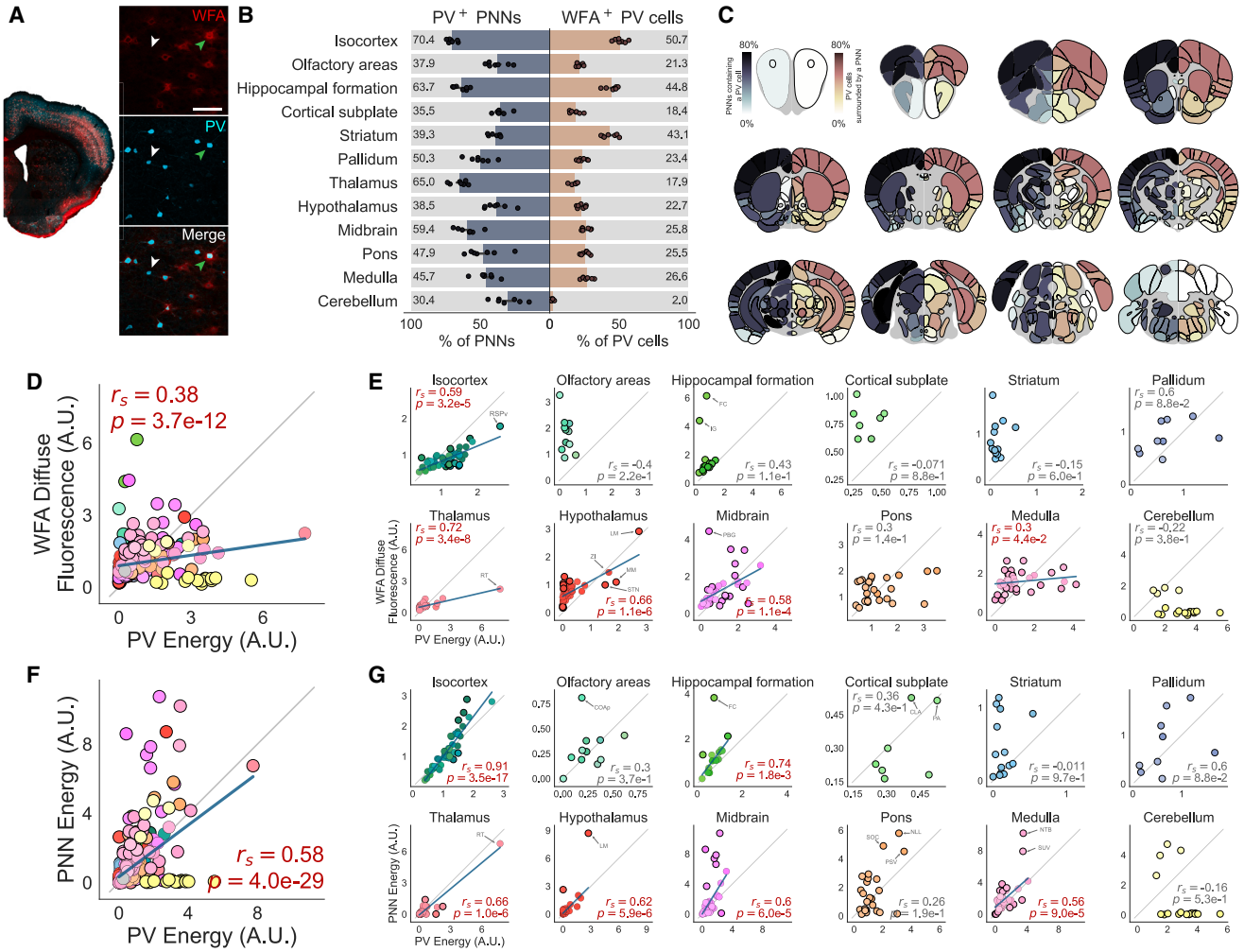

Figure 3. Brain-wide interactions between PNNs and PV cells

(A) Representative image (WFA, red; PV, cyan). Arrowheads show examples of PV cells without a PNN (white) and colocalized PV-PNNs (green). Scale bar, 100 μm.

(B) Colocalization percentages across 12 major brain subdivisions (on the left, the fraction of PNNs containing a PV cell; on the right, the fraction of PV cells surrounded by a PNN).

(C) Heatmaps showing coronal sections of the brain at different anteroposterior locations. Left hemisphere, the percentage of PNNs containing a PV cell; right hemisphere, the percentage of PV cells surrounded by a PNN.

(D) WFA diffuse fluorescence versus PV energy for all brain areas at a mid-ontology level.

(E) Same as in (D), but areas are split in each major brain subdivision.

(F) WFA energy versus PV energy for brain areas at a mid-ontology level.

(G) Same as in (F), but areas are split in each major brain subdivision. Error bars in (B) represent SEM across mice. Dots in (B) represent mice, while in (D–F) and (G) they represent brain areas. Text insets in (D–F) and (G) indicate the Spearman correlation coefficient (r_s) and the corresponding p value, gray line indicates the X-Y bisector, and, for significant correlations highlighted in red, the blue line shows the best linear fit.

It has been previously reported that two distinct network configurations of PV cells might exist, one more permissive toward plasticity and characterized by weak expression of PV (low PV) and another that limits plasticity and with strong PV expression (high PV).[43] These two subpopulations likely reflect distinct timing of neurogenesis and connectivity.[44] Thus, we decided to further explore the relationship between PNNs and PV staining intensity at the level of single cells (Figures 4A and 4B). To do this, we grouped all PV cells in four intensity classes of equal width and measured the probability of being surrounded by a PNN as a function of PV cell intensity. Overall, we found that, as PV intensity increased, the probability of having a PNN increased (Figure 4C). Repeating the analysis for each brain subdivision, we found that the effect was present in all 12 brain macrostructures except for the hypothalamus, which showed a similar but not statistically significant trend, and the cerebellum (Figure 4D). However, the magnitude of such dependency appears to follow three distinct patterns (Figure 4E). In isocortex, striatum, and hippocampal formation, PNN aggregation was strongly and robustly

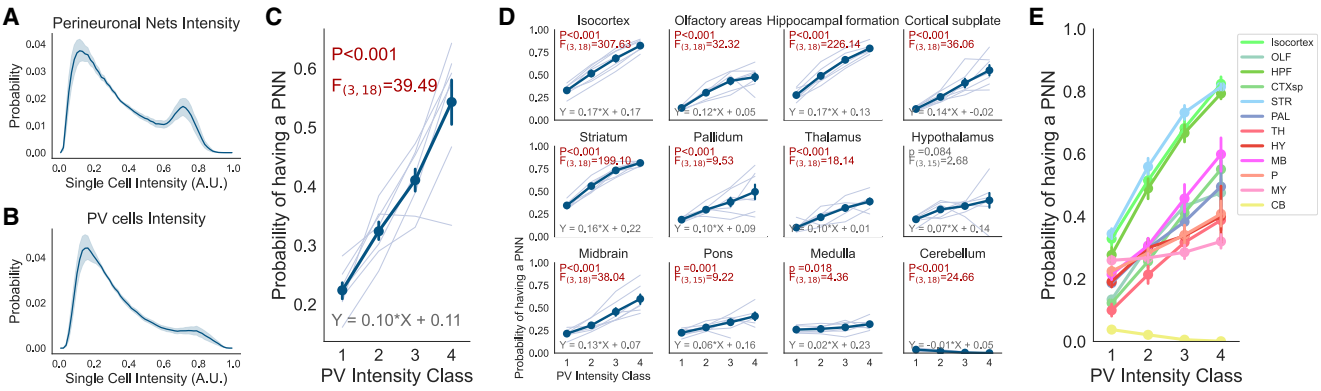

Figure 4. PNN aggregation depends on PV expression levels

(A) Probability density function of the intensity of all PNNs. The thick line represents the average, while shading represents SEM across mice (n = 7 mice, 69,926 ± 5,235 PNNs per mouse).

(B) Same as in (A) but for PV cells (n = 7 mice, 136,479 ± 11,839 PV cells per mouse).

(C) Probability that a PV cell is surrounded by a PNN as a function of PV intensity class (1, low; 2, intermediate-low; 3, intermediate-high; 4, high) calculated for the whole brain.

(D) Same as in (C) but split in each major brain subdivision.

(E) Same as in (D) but all regions are plotted on the same axis. Text insets indicate the result of a one-way RM ANOVA (F statistics and the corresponding p value) and the estimated parameters of the best first-degree linear fit. Thin lines in (C) and (D) represent single mice. Error bars in (C–E) represent SEM across mice.

dependent on PV expression. The relationship was inverse in the cerebellum, likely due to the presence of PV-expressing Purkinje cells, and its strength was only moderate for all the other brain areas.

Overall, these data indicate the existence of a mechanism coupling PV expression with PNN formation. However, the strength of this regulatory mechanism is variable across the brain.

Primary sensory areas share high levels of PNNs

The precise functional role of PNNs in the cerebral cortex is intensely studied.[13] We reasoned that, by analyzing their expression pattern throughout this anatomical district, we could highlight principles of organization that might explain the spatially inhomogeneous distribution of PNNs. Furthermore, the cerebral cortex is divided into layers with different functional properties and PNN expression. We thus plotted WFA diffuse fluorescence and PNN energy in all cortical regions divided by layer (Figure 5A). We noticed that four main groups of regions were characterized by a stronger diffuse WFA staining: somatosensory, visual, and auditory areas, and the retrosplenial cortex (Figure 5A). When analyzing PNN energy, this pattern was much sharper and more localized in layer 4 (Figure 5A, bottom heatmap). Interestingly, while PNN energy was particularly high in primary sensory areas (VISp, AUDp, and all SSp areas) the same enrichment was milder for PV energy (Figure 5B). To further investigate this pattern, we compared, for each sensory system, the aggregated data of primary versus associative cortical regions. In the visual cortex, both diffuse fluorescence and PNN energy were lower in associative (VISpor, VISli, VISl, VISpl, VISpm, VISal, VISam, VISrl, VISa) than in primary (VISp) areas (Figure 5C). This effect was prominent in layer 4 but also present in layers 5 and 6 (Figures 5D and S6A). An analogous difference was present in auditory (Figures 5E, 5F, and S6B) primary (AUDp) versus associative (AUDv, AUDd, AUDpo), and somatosensory areas (Figures 5G, 5H, and S6C) primary (SSp-n, SSp-bfd, SSp-ll, SSp-m, SSp-ul, SSp-tr, SSp-un) versus associative (SSs) with the exception of diffuse fluorescence in the somatosensory regions of the cortex (Figure 5G).

These results indicate that layers 4–5 of primary cortical regions are privileged sites of PNN expression across multiple sensory systems.

Determinants of cortical expression of PNNs: Role of PV cells and area connectivity

Considering the intimate relationship between PV cells and PNNs in the cortex (Figures 3G and 4D), the high expression of PNNs in primary areas could mirror the distribution of PV cells. However, PV energy was only slightly increased in primary visual and auditory, but not somatosensory, cortices (Figures 5B, S6D, S6G, and S6J). Accordingly, splitting data by layers did not reveal any difference between primary and associative regions for all the metrics with the exception of PV energy in deep layers of the visual cortex (Figures S6E, S6F, S6H, S6I, S6K, and S6L). Intriguingly, we observed that PV cells in primary sensory cortices were more likely to have PNNs than in secondary areas (Figures S7A, S7C, and S7E). This effect was not due to a higher proportion of high-PV cells in primary versus associative areas (Figures S7B, S7D, and S7F), suggesting that the mechanism by which PNNs are increased in primary regions could not solely involve PV expression levels.

The high levels of PNNs in layer 4 of primary sensory cortices could be related to the control of feedforward sensory thalamic inputs that densely innervate layer 4 of primary sensory regions.[45] If this hypothesis were true, one should expect PNN energy to scale with thalamic innervation density across sensory areas. Thus, we used published data from the mouse brain connectivity atlas of the Allen Institute[46] to measure thalamic input

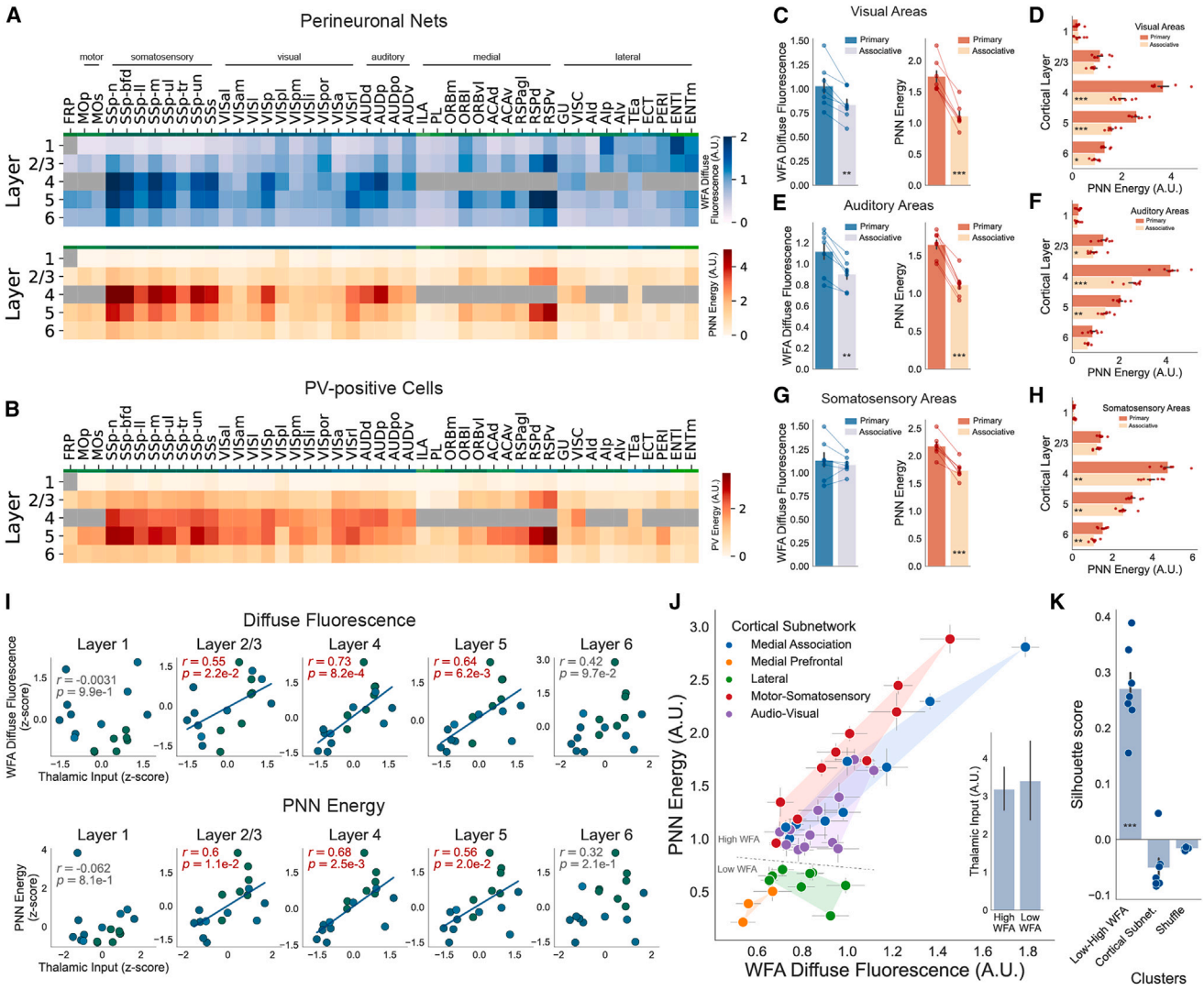

Figure 5. Organization of PNNs in cortical areas

(A) Heatmaps representing average WFA diffuse fluorescence and PNN energy (area acronyms in Table S3). Layer 4 of brain regions that do not have layer 4 is grayed out.

(B) Same as in (A) but for PV energy.

(C) WFA diffuse fluorescence and PNN energy in the primary visual cortex versus higher-order associative visual areas.

(D) PNN energy in primary versus associative visual cortical areas split by layer.

(E) Same as in (C) but for auditory areas.

(F) Same as in (D) but for auditory areas.

(G) Same as in (C) but for somatosensory areas.

(H) Same as in (D) but for somatosensory areas.

(I) Correlation between WFA diffuse fluorescence (top) and PNN energy (bottom) with thalamic input strength in sensory-related areas of the cortex (all somatosensory, visual, and auditory cortices, see STAR Methods) split by layer. Text insets indicate the Pearson's correlation coefficient (*r*) and the corresponding p value. For significant correlations, highlighted in red, the blue line shows the best linear fit.

(J) Scatterplot of PNN energy vs. WFA diffuse fluorescence for all cortical areas colored by their cortical subnetwork. The transparent shading represents the convex hull of all points in a subnetwork. Regions cluster into two groups: high WFA and low WFA. The inset shows the average thalamic input strength of regions divided into high- and low-WFA groups.

(K) Silhouette score calculated for each mouse by grouping cortical areas in two groups (low-high WFA), five groups (cortical Subnet.), or two groups but randomly shuffled (shuffle). In (C–H) and (K), dots represent mice. In (I) and (J), dots represent brain areas. Error bars in (C–H), (J), and (K) represent SEM across mice. Error bars in (J) (inset) represent SEM across brain regions. See Table S1 for statistical comparisons.

strength for all somatosensory, visual, and auditory areas (total inputs from the sensory-motor cortex-related portion of the thalamus, DORsm in the CCFv3 nomenclature, see section ''correlation with thalamic afferent connectivity'' in STAR Methods). Strikingly, we found that both WFA diffuse fluorescence and PNN energy in cortical layers 2/3, 4, and 5 were highly correlated with thalamic input strength, and this effect was most prominent in layer 4 where thalamic afferents could explain respectively 53% and 46% of the variance in the two PNN metrics (r = 0.73 and 0.68) (Figure 5I). As a control, we performed the same analysis with connections originating from the associative cortex-related regions of the thalamus (DORpm) and we found no correlation with PNNs in any cortical layer (Figures S7I and S7J). Thus, thalamic connectivity represents another determinant of PNN abundance, independent from PV expression. Furthermore, these data corroborate the possibility that PNNs could be important for the regulation of sensorimotor thalamic inputs across multiple sensory modalities, and they may provide a basis to investigate the role of PNNs on feedforward functional signaling in sensory cortices.

If connections represent a determinant factor for PNN abundance, it could be that groups of highly interconnected cortical regions have co-regulated levels of PNNs. Recent work clustered the cerebral cortex in five distinct functional subnetworks based on their intracortical connections.[40,47] We used this classification to explore whether PNNs were differentially expressed in these subnetworks. We found that cortical subnetworks were clustered in two groups, with no overlap: a low-WFA group comprising the lateral and medial prefrontal subnetworks and a high-WFA group comprising audiovisual, motor-somatosensory, and medial association networks (Figure 5J). To quantify cluster separation, we grouped brain regions using three strategies: the high/low WFA as described above, the original five cortical subnetworks, and high/low-WFA regions randomly shuffled. For each grouping, we calculated the silhouette score, a metric representing the separation and quality of data clustering.[48] We found that grouping cortical regions in high and low WFA resulted in the highest score (Figure 5K). The subdivision in high- and low-WFA-region groups could not be explained simply by different thalamic input density, since we did not observe any significant difference in the overall thalamocortical connectivity between these two groups of regions in the Allen Institute dataset (Figure 5J, inset). Conversely, we noticed that high-WFA areas also displayed increased PV energy and an increased proportion of high-PV cells (Figure S7G and S7H), suggesting that the different PNN distribution across cortical subnetworks might be instructed by PV cells. These results show that each cortical network displays a typical and homogeneous PNN aggregation and that PV cells and PV expression level contribute to generating cortical PNN distribution.

In summary, these data indicate that two independent regulatory factors, i.e., thalamic input and PV expression, contribute to generate the pattern of PNN expression in the cortex.

Gene expression correlates of PNNs

Finally, we asked whether PNN abundance could be correlated with gene expression patterns. To answer this question, we analyzed the whole-brain gene expression data published by the Allen Institute.[38] This dataset describes region-specific expression levels for about 18,000 genes. For each gene, we correlated its expression in all the brain areas with a metric for PNN staining to detect genes whose pattern of expression is predictive of PNN presence. We found about 5,000 genes positively correlated and about 1,000 negatively correlated with WFA (false discovery rate [FDR] <0.01, Benjamini-Hochberg; see section ''correlation with gene expression and gene set overrepresentation analysis'' in STAR Methods, and Data S4). It is important to note that this analysis reflects gene expression and PNNs at the level of brain areas and not single cells. To validate our approach, we selected a few genes known to be related to PNN structure and function: Aggrecan (*Acan*), a major proteoglycan core protein present in PNNs[11,13,29,49–51]; *Hapln1*, coding for a link protein essential for PNNs structure[10]; hyaluronan synthase 3 (*Has3*), a necessary component for PNN aggregation[12]; matrix metallopeptidase 9 (*Mmp9*), an enzyme known to regulate PNN and PV development[52]; A disintegrin and metalloproteinase with thrombospondin motifs (*Adamts5* also known as *Adamts11*), an aggrecan-degrading protease[53] that is expressed by PV interneurons with a PNN[54]; and parvalbumin (*Pvalb*). All these genes were significantly correlated with both PNN energy and WFA diffuse fluorescence (Figures 6A and 6B). Strikingly, out of 17,639 genes, *Acan* was respectively the second and fifth most correlated gene with WFA diffuse fluorescence (r_s = 0.58) and PNN energy (r_s = 0.57). Consistently, when we repeated this analysis for PV energy, we found that the most correlated gene was *Pvalb* itself (r_s = 0.81). Other markers associated with PV neurons were also positively correlated (Figure 6C). These included the genes encoding the fast voltage-gated potassium channels Kv3.1 and Kv1.1 (*Kcnc1* and *Kcna1*)[55,56] and the sodium channel Nav1.1 (*Scn1A*)[57]; synaptotagmin 2 (*Syt2*), a protein that ensures fast calcium sensing and vesicle release[58]; and *Acan*. These results validated our approach, allowing us to provide lists of positively and negatively correlated genes that might highlight molecular regulators of PNNs. A detailed list of all 17,639 genes and their correlation with PNN and PV staining is available in Data S4.

To obtain insight into the biological processes of the correlated genes, we performed a Gene Ontology analysis separately on the lists of the top 1,000 most correlated and anticorrelated genes with PNN energy, ranked by their correlation coefficient (Figures 6D and 6E). Genes related to processes of axon ensheathment, myelination, mitochondrial function, and cellular respiration were enriched in the pool of the positively correlated transcripts. Conversely, we found that anticorrelated genes were related to processes involved in synaptic plasticity, including postsynaptic density organization, regulation of synapse structure, and learning and memory. This is consistent with the known inhibitory role of PNNs toward synaptic plasticity.[13] Finally, we performed a similar overrepresentation analysis on a smaller gene set, the ''matrisome,''[59] containing about 1,000 genes related to different categories of ECM structure and function. Only the category proteoglycans was strongly overrepresented in the set of positively correlated genes (Figure 6F).

Taken together, these data show that we can reliably identify gene expression correlates of PNN abundance with the approach described above. Moreover, this analysis and the

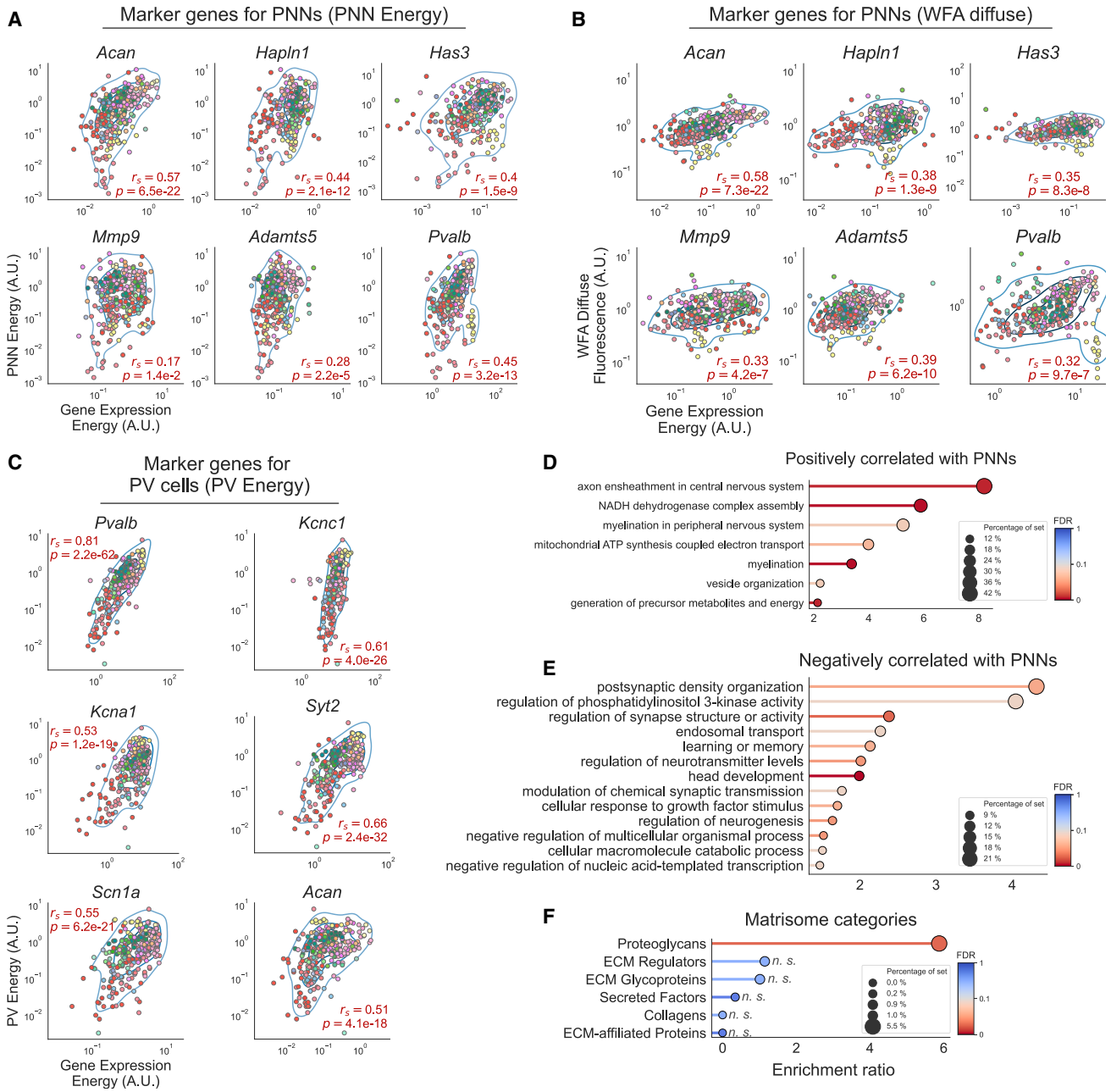

Figure 6. Gene expression correlates of PNNs

(A) Correlation between PNN energy and gene expression for six marker genes: *Acan*, *Hapln1*, *Has3*, *Mmp9*, *Adamts5*, and *Pvalb*. Red text insets indicate the Spearman correlation coefficient (r_s), and p value. To visualize datapoint density, we included blue contour lines representing kernel density estimations.

(B) Same as in (A) but for WFA diffuse fluorescence.

(C) Correlation between PV energy and gene expression for six marker genes: *Pvalb*, *Kcnc1*, *Kcna1*, *Syt2*, *Scn1a*, and *Acan*. To visualize datapoint density, we included blue contour lines representing kernel density estimations.

(D) Biological process terms enriched in genes positively correlated with PNN energy (FDR < 0.1). Data in (D–F) are presented in descending order of enrichment ratio, colored based on the FDR value with darker red shades corresponding to more significant values. The dot size represents the percentage of genes of each category present in the experimental gene list.

(E) Biological process terms enriched in genes negatively correlated with PNN energy. Other conventions as in (D).

(F) The matrisome category Proteoglycans was significantly enriched in the list of genes positively correlated with PNN energy. Other categories not significant (n.s.). Other conventions as in (D).

resulting gene lists could prove useful for designing experiments to investigate the molecular biology underlying PNN development and regulation.

DISCUSSION

Our study reports a whole-brain dataset of PNNs and PV cells in the adult mouse brain. We provide several quantitative measurements of the abundance of PNNs and PV cells and their colocalization in over 600 brain regions. The atlas was built using a shared spatial framework that facilitates replication studies and allows analyzing PNN data together with publicly available connectomics[46,47] and gene expression[38] datasets, which enabled us to identify potential principles of PNN organization and gene expression profiles that are correlated or anticorrelated with PNN abundance. Previous studies have analyzed PNNs in multiple brain regions[11,29]; however, they have been limited by their focus on only a subset of areas, their use of a more qualitative approach, or their use of a non-standard reference volume. In contrast, our atlas addresses all these aspects.

Our public resources (Data S1–4) will help researchers to generate hypotheses and questions and to design experiments to better understand the function of PNNs and their involvement in pathological conditions. One of the challenges in studying PNNs is the difficulty of automatically detecting them due to their high morphological variability. To address this issue, we released two deep-learning models for the detection of PNNs and PV cells, pre-trained on about 0.8 million manually annotated PNNs/cells. The models can also be fine-tuned to specific experimental needs and image qualities with additional training. We have also made all of the raw and processed data from this study freely available (raw dataset, Zenodo link[60]; prediction images; Zenodo link[61]; processed data, Data S1–4), and developed a web app to browse the data (www.pnnatlas.sns.it).

Diffuse CSPGs and aggregated PNN distributions

CSPGs are large, complex molecules that are widely distributed throughout the brain, whereas PNNs are aggregated around specific neurons.[13] While most research on PNNs has focused on telencephalic structures, our analysis revealed that PNNs are highly abundant in the midbrain and hindbrain (pons and medulla). These areas are important for vital processes such as heartbeat and breathing control, basic reflexes, motor control, and sleep.[62,63] However, the role of PNNs in the neural circuits underlying these functions is largely unknown.

We also found that CSPG aggregation in PNNs may be differentially regulated across brain areas. While, in most of the brain, the amount of non-aggregated CSPGs (diffuse WFA fluorescence) was a good predictor of the presence of aggregated PNNs (PNN energy), some areas showed no relationship between the two metrics. For example, all olfactory areas had very intense diffuse staining but contained very few and thin PNNs (Figures 2A, 2C, and 2E),[64] indicating that the high amount of CSPGs present in these areas did not aggregate into PNNs. This pattern was also observed in the cortical subplate (Figure 2E). The region-specific regulatory mechanisms of CSPG aggregation into PNNs and the functional implications are currently unknown and require further investigation.

PV levels are associated with the presence of PNNs

A commonly observed property of cortical PNNs is that they preferentially aggregate around GABAergic PV-positive interneurons.[13] We measured that, on average, this was the case for about 60% of PNNs in the entire brain, a much higher percentage than expected from chance. Moreover, across the whole brain, both PNN metrics were correlated with PV energy. Despite this clear association, slightly less than half of the PNNs in the brain do not surround PV neurons, leaving the still-unanswered question of whether they might serve to regulate different circuit properties.

The link between PNNs and PV cells also varied between brain subdivisions with the most striking pattern in the isocortex. Here, 70% of all PNNs were around PV cells and half of all PV cells had a net. This intimate association was also evident in the relation between staining metrics. Indeed, cortical areas had a very tight (r_s = 0.91) correlation between PNN and PV energy.

Our analysis showed that the probability of being surrounded by a PNN for a PV cell is highly dependent on its PV expression level. This is consistent with previous reports in the prelimbic cortex showing a positive correlation between PV and WFA staining intensity.[65] Given that PV neurons differentiate before birth[66] and PNNs aggregate much later during postnatal development,[8] this association suggests that the developmental increase in PV expression enhances the probability to develop a PNN.

The magnitude of the association between PV levels and the probability of having a PNN, however, varies across brain structures, suggesting that the mechanism that couples PV expression to PNN aggregation can be fine-tuned. For example, in the isocortex, hippocampal formation, and striatum, PV-PNN coupling was particularly strong. Intriguingly, in all three of these brain regions, PV cells have been previously divided, based on their intensity, into two distinct subpopulations of early-born high-PV cells and late-born low-PV cells with different roles in plasticity and learning.[43,44] Our data are consistent with the interpretation that PNNs might aggregate more onto early-born high-PV neurons contributing to the inhibitory role of this subpopulation toward plasticity. In summary, it is currently unknown how perineuronal nets and parvalbumin are co-regulated. Previous evidence suggests that Otx2 may act as a mediator of this coupling, promoting the maturation of PV cells and PNNs.[67,68] Further research is needed to confirm this hypothesis.

PNN expression in the cortex is correlated with specific connectivity patterns

Our study demonstrated that strong PNNs are a common feature of layer 4 in all primary sensory cortices. This enrichment was evident also when we directly compared the labeling of primary and associative cortices within each sensory modality. Interestingly, this pattern cannot be explained solely by an increase in the number of PV cells or in the proportion of high-PV cells that are more likely to have a PNN. At a functional level, the high expression of PNNs in primary sensory areas could be related to their action on thalamic afferents. Previous research in the mouse primary visual cortex showed that PNNs can selectively control thalamic excitation onto PV cells.[45] Our data suggest

that the control of feedforward thalamo-cortical sensory inputs on PV neurons may be one important function across all sensory cortices. This is supported by the observation that the abundance of PNNs correlates with the density of thalamic innervation in all sensory areas. This hypothesis is also in accordance with the findings that plasticity in L4 of the visual cortex is lower[69] and might rely on separate molecular mechanisms.[70]

The relationship between thalamic inputs and PNN levels raises the possibility that the type of connections may be a determining factor in PNN expression. This idea was further supported by the observation that regions of the cortex with strong PV and PNN expression tend to have similar intracortical connectivity patterns (Figure 5J). This finding suggests that circuitry within these areas requires a certain level of stability, which could be achieved through the expression of PNNs. This concept merits further investigation to fully understand how this relationship functions.

Gene expression correlates of PNNs

The search for a gene expression signature of PNN-enwrapped cells is hampered by the fact that PNNs are extracellular multimolecular structures and that there is currently no means to tag the PNN-positive neurons.

To overcome this problem, we performed a correlational analysis between the dataset by the Allen Institute[38] and PNN expression. This approach was validated by the overrepresentation analysis on the matrisome gene set, which showed that PNN-correlated genes are strongly enriched in the proteoglycan category, and by finding key constituents of the PNN ranking in the top positions of the list of genes positively correlated with PNN energy. However, this approach also revealed many other genes with positive and negative correlations with PNNs. A Gene Ontology analysis strikingly showed that categories related to synaptic function and synaptic plasticity were significantly downregulated in brain areas enriched with PNNs. Furthermore, PNNs were found to be correlated with genes involved in myelination, another plasticity brake,[71,72] and genes related to cell metabolism, which may be due to the high energy demands of fast-spiking PV cells.[73,74]

These results not only support the hypothesis that PNNs serve as plasticity brakes in the visual cortex[13] but also demonstrate that this functional signature emerges from an unbiased comprehensive analysis of all brain regions.

Our work adopts an approach based on a brain-wide comparison of very large datasets of cellular structures with public resources. This type of analysis has the advantage of being unbiased and data driven, which is typical of omics techniques. It can also be applied to the study of many other extracellular matrix components. We envision that the advent of spatial transcriptomics will further enhance this type of approach.

Limitations of the study

In interpreting our results, it is important to note that we used WFA as a marker for PNNs. While WFA is a commonly used method for visualizing PNNs,[13] it does not equally bind to all structures of aggregated CSPGs. Therefore, the use of other antibodies that specifically target different proteoglycans may be necessary to fully reveal the presence of these structures.[1,29,75,76] Our approach can be easily adapted to count these different types of PNNs, creating brain atlases of all the major components of PNNs. Additionally, colocalization with other cell types could also be studied. For example, PV-positive neurons are a heterogeneous population[77] that cannot be distinguished using our immunofluorescence approach. However, specific promoters and enhancers could be used to label PV-cell subtypes in a brain-wide manner, allowing the study of their colocalization with PNNs and a more detailed understanding of PNN expression regulation.

Another limitation of our study is that the number of subjects was not sufficient for stratification of our data by sex. However, we ensured general validity by analyzing a balanced number of male and female mice. Additionally, as our atlas is highly standardized, any new sex-specific data can be easily added to the existing datasets.

STAR★METHODS

Detailed methods are provided in the online version of this paper and include the following:

- KEY RESOURCES TABLE
- RESOURCE AVAILABILITY
  - Lead contact
  - Materials availability
  - Data and code availability
- EXPERIMENTAL MODEL AND SUBJECT DETAILS
  - Animals
- METHOD DETAILS
  - Immunofluorescence staining
  - Image acquisition
  - Image registration to the Allen Brain Atlas CCFv3-2017
  - Deep learning models for cell counting
  - Brain structure sets
- QUANTIFICATION AND STATISTICAL ANALYSIS
  - Measurement of single-cell staining intensity
  - Staining metrics definitions
  - Colocalization PNN-PV
  - PV intensity classes
  - Correlation between staining metrics
  - Correlation with thalamic afferent connectivity
  - Correlation with gene expression and gene set overrepresentation analysis
  - Data visualization

SUPPLEMENTAL INFORMATION

Supplemental information can be found online at https://doi.org/10.1016/j.celrep.2023.112788.

ACKNOWLEDGMENTS

This work was funded by AI4Media - A European Excellence Centre for Media, Society and Democracy (EC, H2020 n. 951911); the Tuscany Health Ecosystem (THE) Project (CUP I53C22000780001), funded by the National Recovery and Resilience Plan (NRPP), within the NextGeneration Europe (NGEU) Program; the CRONOLAB project of the PRO3 joint program; and PRIN2017 2017HMH8FA to T.P. R.M. was supported by Fondazione Umberto Veronesi.

We thank Silvia Burchielli, Cecilia Ciampi, Domiziana Terlizzi, Francesca Biondi, Sara Ciampi, and Elena Novelli for technical support and Cristiano Ricci, Francesco Calugi, Giulia Sagona, Elsa Ghirardini, Laura Baroncelli, Francesca Damiani, Matteo Alberti, Andrea Tognozzi, Maria Grazia Giuliano, and Matteo Caldarelli for scientific discussions.

AUTHOR CONTRIBUTIONS

Conceptualization, L.L., V.T., T.P., and R.M.; methodology, L.L., V.T., L.C., and F.C.; software, L.L., V.T., L.C., and F.C.; validation, L.L., V.T., L.C., and F.C.; formal analysis, L.L. and V.T.; investigation, L.L., V.T., and S.C.; resources, T.P., P.T., C.G., G.A., and R.M.; data curation, V.T., E.G., L.L., S.C., A.V., F.T., E.P., R.M., and T.P.; writing – original draft, L.L., T.P., V.T., and F.C.; writing – review & editing, L.L., V.T., T.P., F.C., R.M., C.G., and P.T.; visualization, L.L., V.T., and F.C.; supervision, T.P., P.T., C.G., G.A., and R.M.; project administration, T.P.; funding acquisition, T.P., G.A., C.G., and F.C.

DECLARATION OF INTERESTS

The authors declare no competing interests.

INCLUSION AND DIVERSITY

We support inclusive, diverse, and equitable conduct of research. We worked to ensure sex balance in the selection of non-human subjects.

Received: February 8, 2023
Revised: May 3, 2023
Accepted: June 25, 2023
Published: July 11, 2023

REFERENCES

1. Galtrey, C.M., Kwok, J.C.F., Carulli, D., Rhodes, K.E., and Fawcett, J.W. (2008). Distribution and synthesis of extracellular matrix proteoglycans, hyaluronan, link proteins and tenascin-R in the rat spinal cord. Eur. J. Neurosci. *27*, 1373–1390.
2. Hendry, S.H., Jones, E.G., Hockfield, S., and McKay, R.D. (1988). Neuronal populations stained with the monoclonal antibody Cat-301 in the mammalian cerebral cortex and thalamus. J. Neurosci. *8*, 518–542.
3. Köppe, G., Brückner, G., Brauer, K., Härtig, W., and Bigl, V. (1997). Developmental patterns of proteoglycan-containing extracellular matrix in perineuronal nets and neuropil of the postnatal rat brain. Cell Tissue Res. *288*, 33–41.
4. Seeger, G., Brauer, K., Härtig, W., and Brückner, G. (1994). Mapping of perineuronal nets in the rat brain stained by colloidal iron hydroxide histochemistry and lectin cytochemistry. Neuroscience *58*, 371–388.
5. Boggio, E.M., Ehlert, E.M., Lupori, L., Moloney, E.B., De Winter, F., Vander Kooi, C.W., Baroncelli, L., Mecollari, V., Blits, B., Fawcett, J.W., et al. (2019). Inhibition of Semaphorin3A Promotes Ocular Dominance Plasticity in the Adult Rat Visual Cortex. Mol. Neurobiol. *56*, 5987–5997.
6. Lensjø, K.K., Lepperød, M.E., Dick, G., Hafting, T., and Fyhn, M. (2017). Removal of Perineuronal Nets Unlocks Juvenile Plasticity Through Network Mechanisms of Decreased Inhibition and Increased Gamma Activity. J. Neurosci. *37*, 1269–1283.
7. Pizzorusso, T., Medini, P., Berardi, N., Chierzi, S., Fawcett, J.W., and Maffei, L. (2002). Reactivation of Ocular Dominance Plasticity in the Adult Visual Cortex. Science *298*, 1248–1251.
8. Reichelt, A.C., Hare, D.J., Bussey, T.J., and Saksida, L.M. (2019). Perineuronal Nets: Plasticity, Protection, and Therapeutic Potential. Trends Neurosci. *42*, 458–470.
9. Ye, Q., and Miao, Q.-l. (2013). Experience-dependent development of perineuronal nets and chondroitin sulfate proteoglycan receptors in mouse visual cortex. Matrix Biol. *32*, 352–363.
10. Carulli, D., Pizzorusso, T., Kwok, J.C.F., Putignano, E., Poli, A., Forostyak, S., Andrews, M.R., Deepa, S.S., Glant, T.T., and Fawcett, J.W. (2010). Animals lacking link protein have attenuated perineuronal nets and persistent plasticity. Brain *133*, 2331–2347.
11. Dauth, S., Grevesse, T., Pantazopoulos, H., Campbell, P.H., Maoz, B.M., Berretta, S., and Parker, K.K. (2016). Extracellular matrix protein expression is brain region dependent. J. Comp. Neurol. *524*, 1309–1336.
12. Kwok, J.C.F., Carulli, D., and Fawcett, J.W. (2010). In vitro modeling of perineuronal nets: hyaluronan synthase and link protein are necessary for their formation and integrity. J. Neurochem. *114*, 1447–1459.
13. Fawcett, J.W., Oohashi, T., and Pizzorusso, T. (2019). The roles of perineuronal nets and the perinodal extracellular matrix in neuronal function. Nat. Rev. Neurosci. *20*, 451–465.
14. Härtig, W., Derouiche, A., Welt, K., Brauer, K., Grosche, J., Mäder, M., Reichenbach, A., and Brückner, G. (1999). Cortical neurons immunoreactive for the potassium channel Kv3.1b subunit are predominantly surrounded by perineuronal nets presumed as a buffering system for cations. Brain Res. *842*, 15–29.
15. Fawcett, J.W., Fyhn, M., Jendelova, P., Kwok, J.C.F., Ruzicka, J., and Sorg, B.A. (2022). The extracellular matrix and perineuronal nets in memory. Mol. Psychiatry *27*, 3192–3203.
16. Nabel, E.M., and Morishita, H. (2013). Regulating Critical Period Plasticity: Insight from the Visual System to Fear Circuitry for Therapeutic Interventions. Front. Psychiatry *4*, 146.
17. Beurdeley, M., Spatazza, J., Lee, H.H.C., Sugiyama, S., Bernard, C., Di Nardo, A.A., Hensch, T.K., and Prochiantz, A. (2012). Otx2 Binding to Perineuronal Nets Persistently Regulates Plasticity in the Mature Visual Cortex. J. Neurosci. *32*, 9429–9437.
18. Miyata, S., Komatsu, Y., Yoshimura, Y., Taya, C., and Kitagawa, H. (2012). Persistent cortical plasticity by upregulation of chondroitin 6-sulfation. Nat. Neurosci. *15*, 414–422.
19. Rowlands, D., Lensjø, K.K., Dinh, T., Yang, S., Andrews, M.R., Hafting, T., Fyhn, M., Fawcett, J.W., and Dick, G. (2018). Aggrecan Directs Extracellular Matrix-Mediated Neuronal Plasticity. J. Neurosci. *38*, 10102–10113.
20. Gogolla, N., Caroni, P., Lüthi, A., and Herry, C. (2009). Perineuronal Nets Protect Fear Memories from Erasure. Science *325*, 1258–1261.
21. Poli, A., Viglione, A., Mazziotti, R., Totaro, V., Morea, S., Melani, R., Silingardi, D., Putignano, E., Berardi, N., and Pizzorusso, T. (2023). Selective Disruption of Perineuronal Nets in Mice Lacking Crtl1 is Sufficient to Make Fear Memories Susceptible to Erasure. Mol. Neurobiol. *60*, 4105–4119.
22. Christensen, A.C., Lensjø, K.K., Lepperød, M.E., Dragly, S.-A., Sutterud, H., Blackstad, J.S., Fyhn, M., and Hafting, T. (2021). Perineuronal nets stabilize the grid cell network. Nat. Commun. *12*, 253.
23. Carulli, D., Broersen, R., de Winter, F., Muir, E.M., Mešković, M., de Waal, M., de Vries, S., Boele, H.-J., Canto, C.B., De Zeeuw, C.I., and Verhaagen, J. (2020). Cerebellar plasticity and associative memories are controlled by perineuronal nets. Proc. Natl. Acad. Sci. USA *117*, 6855–6865.
24. Cope, E.C., Zych, A.D., Katchur, N.J., Waters, R.C., Laham, B.J., Diethorn, E.J., Park, C.Y., Meara, W.R., and Gould, E. (2022). Atypical perineuronal nets in the CA2 region interfere with social memory in a mouse model of social dysfunction. Mol. Psychiatry *27*, 3520–3531.
25. Domínguez, S., Rey, C.C., Therreau, L., Fanton, A., Massotte, D., Verret, L., Piskorowski, R.A., and Chevaleyre, V. (2019). Maturation of PNN and ErbB4 Signaling in Area CA2 during Adolescence Underlies the Emergence of PV Interneuron Plasticity and Social Memory. Cell Rep. *29*, 1099–1112.e4.
26. Bradbury, E.J., Moon, L.D.F., Popat, R.J., King, V.R., Bennett, G.S., Patel, P.N., Fawcett, J.W., and McMahon, S.B. (2002). Chondroitinase ABC promotes functional recovery after spinal cord injury. Nature *416*, 636–640.
27. Cabungcal, J.-H., Steullet, P., Morishita, H., Kraftsik, R., Cuenod, M., Hensch, T.K., and Do, K.Q. (2013). Perineuronal nets protect fast-spiking interneurons against oxidative stress. Proc. Natl. Acad. Sci. USA *110*, 9130–9135.

28. Pantazopoulos, H., Woo, T.-U.W., Lim, M.P., Lange, N., and Berretta, S. (2010). Extracellular matrix-glial abnormalities in the amygdala and entorhinal cortex of subjects diagnosed with schizophrenia. Arch. Gen. Psychiatry *67*, 155–166.

29. Ueno, H., Fujii, K., Suemitsu, S., Murakami, S., Kitamura, N., Wani, K., Aoki, S., Okamoto, M., Ishihara, T., and Takao, K. (2018). Expression of aggrecan components in perineuronal nets in the mouse cerebral cortex. IBRO Rep. *4*, 22–37.

30. Carstens, K.E., Phillips, M.L., Pozzo-Miller, L., Weinberg, R.J., and Dudek, S.M. (2016). Perineuronal Nets Suppress Plasticity of Excitatory Synapses on CA2 Pyramidal Neurons. J. Neurosci. *36*, 6312–6320.

31. Wingert, J.C., and Sorg, B.A. (2021). Impact of Perineuronal Nets on Electrophysiology of Parvalbumin Interneurons, Principal Neurons, and Brain Oscillations: A Review. Front. Synaptic Neurosci. *13*, 673210.

32. Romberg, C., Yang, S., Melani, R., Andrews, M.R., Horner, A.E., Spillantini, M.G., Bussey, T.J., Fawcett, J.W., Pizzorusso, T., and Saksida, L.M. (2013). Depletion of Perineuronal Nets Enhances Recognition Memory and Long-Term Depression in the Perirhinal Cortex. J. Neurosci. *33*, 7057–7065.

33. Bukalo, O., Schachner, M., and Dityatev, A. (2007). Hippocampal Metaplasticity Induced by Deficiency in the Extracellular Matrix Glycoprotein Tenascin-R. J. Neurosci. *27*, 6019–6028.

34. Ciampi, L., Carrara, F., Totaro, V., Mazziotti, R., Lupori, L., Santiago, C., Amato, G., Pizzorusso, T., and Gennaro, C. (2022). Learning to count biological structures with raters' uncertainty. Med. Image Anal. *80*, 102500.

35. Lipachev, N., Arnst, N., Melnikova, A., Jäälinoja, H., Kochneva, A., Zhigalov, A., Kulesskaya, N., Aganov, A.V., Mavlikeev, M., Rauvala, H., et al. (2019). Quantitative changes in perineuronal nets in development and posttraumatic condition. J. Mol. Histol. *50*, 203–216.

36. Foscarin, S., Ponchione, D., Pajaj, E., Leto, K., Gawlak, M., Wilczynski, G.M., Rossi, F., and Carulli, D. (2011). Experience-Dependent Plasticity and Modulation of Growth Regulatory Molecules at Central Synapses. PLoS One *6*, e16666.

37. Napoli, D., Lupori, L., Mazziotti, R., Sagona, G., Bagnoli, S., Samad, M., Sacramento, E.K., Kirkpartick, J., Putignano, E., Chen, S., et al. (2020). MiR-29 coordinates age-dependent plasticity brakes in the adult visual cortex. EMBO Rep. *21*, e50431.

38. Lein, E.S., Hawrylycz, M.J., Ao, N., Ayres, M., Bensinger, A., Bernard, A., Boe, A.F., Boguski, M.S., Brockway, K.S., Byrnes, E.J., et al. (2007). Genome-wide atlas of gene expression in the adult mouse brain. Nature *445*, 168–176.

39. Bjerke, I.E., Yates, S.C., Laja, A., Witter, M.P., Puchades, M.A., Bjaalie, J.G., and Leergaard, T.B. (2021). Densities and numbers of calbindin and parvalbumin positive neurons across the rat and mouse brain. iScience *24*, 101906.

40. Kim, Y., Yang, G.R., Pradhan, K., Venkataraju, K.U., Bota, M., García Del Molino, L.C., Fitzgerald, G., Ram, K., He, M., Levine, J.M., et al. (2017). Brain-wide Maps Reveal Stereotyped Cell-Type-Based Cortical Architecture and Subcortical Sexual Dimorphism. Cell *171*, 456–469.e22.

41. Baimbridge, K.G., and Miller, J.J. (1982). Immunohistochemical localization of calcium-binding protein in the cerebellum, hippocampal formation and olfactory bulb of the rat. Brain Res. *245*, 223–229.

42. Bastianelli, E. (2003). Distribution of calcium-binding proteins in the cerebellum. Cerebellum *2*, 242–262.

43. Donato, F., Rompani, S.B., and Caroni, P. (2013). Parvalbumin-expressing basket-cell network plasticity induced by experience regulates adult learning. Nature *504*, 272–276.

44. Donato, F., Chowdhury, A., Lahr, M., and Caroni, P. (2015). Early- and Late-Born Parvalbumin Basket Cell Subpopulations Exhibiting Distinct Regulation and Roles in Learning. Neuron *85*, 770–786.

45. Faini, G., Aguirre, A., Landi, S., Lamers, D., Pizzorusso, T., Ratto, G.M., Deleuze, C., and Bacci, A. (2018). Perineuronal nets control visual input via thalamic recruitment of cortical PV interneurons. Elife *7*, e41520.

46. Oh, S.W., Harris, J.A., Ng, L., Winslow, B., Cain, N., Mihalas, S., Wang, Q., Lau, C., Kuan, L., Henry, A.M., et al. (2014). A mesoscale connectome of the mouse brain. Nature *508*, 207–214.

47. Zingg, B., Hintiryan, H., Gou, L., Song, M.Y., Bay, M., Bienkowski, M.S., Foster, N.N., Yamashita, S., Bowman, I., Toga, A.W., and Dong, H.-W. (2014). Neural Networks of the Mouse Neocortex. Cell *156*, 1096–1111.

48. Zhao, S., Sun, J., Shimizu, K., and Kadota, K. (2018). Silhouette Scores for Arbitrary Defined Groups in Gene Expression Data and Insights into Differential Expression Results. Biol. Proced. Online *20*, 5.

49. Härtig, W., Meinicke, A., Michalski, D., Schob, S., and Jäger, C. (2022). Update on Perineuronal Net Staining With Wisteria floribunda Agglutinin (WFA). Front. Integr. Neurosci. *16*, 851988.

50. Oohashi, T., Edamatsu, M., Bekku, Y., and Carulli, D. (2015). The hyaluronan and proteoglycan link proteins: Organizers of the brain extracellular matrix and key molecules for neuronal function and plasticity. Exp. Neurol. *274*, 134–144.

51. Yamada, J., and Jinno, S. (2017). Molecular heterogeneity of aggrecan-based perineuronal nets around five subclasses of parvalbumin-expressing neurons in the mouse hippocampus. J. Comp. Neurol. *525*, 1234–1249.

52. Pirbhoy, P.S., Rais, M., Lovelace, J.W., Woodard, W., Razak, K.A., Binder, D.K., and Ethell, I.M. (2020). Acute pharmacological inhibition of matrix metalloproteinase-9 activity during development restores perineuronal net formation and normalizes auditory processing in Fmr1 KO mice. J. Neurochem. *155*, 538–558.

53. Held-Feindt, J., Paredes, E.B., Blömer, U., Seidenbecher, C., Stark, A.M., Mehdorn, H.M., and Mentlein, R. (2006). Matrix-degrading proteases ADAMTS4 and ADAMTS5 (disintegrins and metalloproteinases with thrombospondin motifs 4 and 5) are expressed in human glioblastomas. Int. J. Cancer *118*, 55–61.

54. Rossier, J., Bernard, A., Cabungcal, J.-H., Perrenoud, Q., Savoye, A., Gallopin, T., Hawrylycz, M., Cuénod, M., Do, K., Urban, A., and Lein, E.S. (2015). Cortical fast-spiking parvalbumin interneurons enwrapped in the perineuronal net express the metallopeptidases Adamts8, Adamts15 and Neprilysin. Mol. Psychiatry *20*, 154–161.

55. Chow, A., Erisir, A., Farb, C., Nadal, M.S., Ozaita, A., Lau, D., Welker, E., and Rudy, B. (1999). K+ Channel Expression Distinguishes Subpopulations of Parvalbumin- and Somatostatin-Containing Neocortical Interneurons. J. Neurosci. *19*, 9332–9345.

56. Lorincz, A., and Nusser, Z. (2008). Cell-Type-Dependent Molecular Composition of the Axon Initial Segment. J. Neurosci. *28*, 14329–14340.

57. Ogiwara, I., Miyamoto, H., Morita, N., Atapour, N., Mazaki, E., Inoue, I., Takeuchi, T., Itohara, S., Yanagawa, Y., Obata, K., et al. (2007). Nav1.1 Localizes to Axons of Parvalbumin-Positive Inhibitory Interneurons: A Circuit Basis for Epileptic Seizures in Mice Carrying an Scn1a Gene Mutation. J. Neurosci. *27*, 5903–5914.

58. Bouhours, B., Gjoni, E., Kochubey, O., and Schneggenburger, R. (2017). Synaptotagmin2 (Syt2) Drives Fast Release Redundantly with Syt1 at the Output Synapses of Parvalbumin-Expressing Inhibitory Neurons. J. Neurosci. *37*, 4604–4617.

59. Naba, A., Clauser, K.R., Ding, H., Whittaker, C.A., Carr, S.A., and Hynes, R.O. (2016). The extracellular matrix: Tools and insights for the "omics" era. Matrix Biol. *49*, 10–24.

60. Lupori, L., Totaro, V., Cornuti, S., Ciampi, L., Carrara, F., Grilli, E., Viglione, A., Tozzi, F., Putignano, E., Mazziotti, R., et al. (2022). A brain-wide, annotated dataset of WFA-positive perineuronal nets and parvalbumin neurons in the adult mouse brain. https://doi.org/10.5281/zenodo.7419282.

61. Lupori, L., Totaro, V., Cornuti, S., Ciampi, L., Carrara, F., Grilli, E., Viglione, A., Tozzi, F., Putignano, E., Mazziotti, R., et al. (2023). A deep learning-based dataset of WFA-positive perineuronal nets and parvalbumin neurons localizations in the adult mouse brain. https://doi.org/10.5281/zenodo.7886214.

62. Ruder, L., Schina, R., Kanodia, H., Valencia-Garcia, S., Pivetta, C., and Arber, S. (2021). A functional map for diverse forelimb actions within brainstem circuitry. Nature *590*, 445–450.

63. Saladin, K.S., Gan, C.A., and Cushman, H.N. (2021). Anatomy & Physiology: The Unity of Form and Function (McGraw-Hill Education). Google-Books-ID: MtFSzQEACAAJ.

64. Hunyadi, A., Gaál, B., Matesz, C., Meszar, Z., Morawski, M., Reimann, K., Lendvai, D., Alpar, A., Wéber, I., and Rácz, É. (2020). Distribution and classification of the extracellular matrix in the olfactory bulb. Brain Struct. Funct. *225*, 321–344.

65. Carceller, H., Guirado, R., Ripolles-Campos, E., Teruel-Marti, V., and Nacher, J. (2020). Perineuronal Nets Regulate the Inhibitory Perisomatic Input onto Parvalbumin Interneurons and γ Activity in the Prefrontal Cortex. J. Neurosci. *40*, 5008–5018.

66. Fishell, G. (2008). Perspectives on the Developmental Origins of Cortical Interneuron Diversity. In Cortical Development: Genes and Genetic Abnormalities (John Wiley & Sons, Ltd), pp. 21–44.

67. Gibel-Russo, R., Benacom, D., and Di Nardo, A.A. (2022). Non-Cell-Autonomous Factors Implicated in Parvalbumin Interneuron Maturation and Critical Periods. Front. Neural Circuits *16*, 875873.

68. Lee, H.H.C., Bernard, C., Ye, Z., Acampora, D., Simeone, A., Prochiantz, A., Di Nardo, A.A., and Hensch, T.K. (2017). Genetic Otx2 mis-localization delays critical period plasticity across brain regions. Mol. Psychiatry *22*. 785–688.

69. Trachtenberg, J.T., Trepel, C., and Stryker, M.P. (2000). Rapid extragranular plasticity in the absence of thalamocortical plasticity in the developing primary visual cortex. Science *287*, 2029–2032.

70. Liu, C.-H., Heynen, A.J., Shuler, M.G.H., and Bear, M.F. (2008). Cannabinoid Receptor Blockade Reveals Parallel Plasticity Mechanisms in Different Layers of Mouse Visual Cortex. Neuron *58*, 340–345.

71. Boghdadi, A.G., Teo, L., and Bourne, J.A. (2018). The Involvement of the Myelin-Associated Inhibitors and Their Receptors in CNS Plasticity and Injury. Mol. Neurobiol. *55*, 1831–1846.

72. Bonetto, G., Belin, D., and Káradóttir, R.T. (2021). Myelin: A gatekeeper of activity-dependent circuit plasticity? Science *374*, eaba6905.

73. Carter, B.C., and Bean, B.P. (2009). Sodium Entry during Action Potentials of Mammalian Neurons: Incomplete Inactivation and Reduced Metabolic Efficiency in Fast-Spiking Neurons. Neuron *64*, 898–909.

74. Kann, O., Papageorgiou, I.E., and Draguhn, A. (2014). Highly Energized Inhibitory Interneurons are a Central Element for Information Processing in Cortical Networks. J. Cereb. Blood Flow Metab. *34*, 1270–1282.

75. Ariza, J., Rogers, H., Hashemi, E., Noctor, S.C., and Martínez-Cerdeño, V. (2018). The Number of Chandelier and Basket Cells Are Differentially Decreased in Prefrontal Cortex in Autism. Cerebr. Cortex *28*, 411–420.

76. Matthews, R.T., Kelly, G.M., Zerillo, C.A., Gray, G., Tiemeyer, M., and Hockfield, S. (2002). Aggrecan glycoforms contribute to the molecular heterogeneity of perineuronal nets. J. Neurosci. *22*, 7536–7547.

77. Tasic, B., Menon, V., Nguyen, T.N., Kim, T.K., Jarsky, T., Yao, Z., Levi, B., Gray, L.T., Sorensen, S.A., Dolbeare, T., et al. (2016). Adult mouse cortical cell taxonomy revealed by single cell transcriptomics. Nat. Neurosci. *19*, 335–346.

78. Carrara, F., Ciampi, L., and Santiago, C. (2022). ciampluca/counting_perineuronal_nets: v0.5. https://doi.org/10.5281/zenodo.7985842.

79. Totaro, V., and Lupori, L. (2023). LeonardoLupori/wholeBrain_PNN_analysis: V0.3.0. https://doi.org/10.5281/zenodo.7991607.

80. Berg, S., Kutra, D., Kroeger, T., Straehle, C.N., Kausler, B.X., Haubold, C., Schiegg, M., Ales, J., Beier, T., Rudy, M., et al. (2019). ilastik: interactive machine learning for (bio)image analysis. Nat. Methods *16*, 1226–1232.

81. Wang, Q., Ding, S.-L., Li, Y., Royall, J., Feng, D., Lesnar, P., Graddis, N., Naeemi, M., Facer, B., Ho, A., et al. (2020). The Allen Mouse Brain Common Coordinate Framework: A 3D Reference Atlas. Cell *181*, 936–953.e20.

82. Puchades, M.A., Csucs, G., Ledergerber, D., Leergaard, T.B., and Bjaalie, J.G. (2019). Spatial registration of serial microscopic brain images to three-dimensional reference atlases with the QuickNII tool. PLoS One *14*, e0216796.

83. Ren, S., He, K., Girshick, R., and Sun, J. (2017). Faster R-CNN: Towards Real-Time Object Detection with Region Proposal Networks. IEEE Trans. Pattern Anal. Mach. Intell. *39*, 1137–1149.

84. Harris, C.R., Millman, K.J., van der Walt, S.J., Gommers, R., Virtanen, P., Cournapeau, D., Wieser, E., Taylor, J., Berg, S., Smith, N.J., et al. (2020). Array programming with NumPy. Nature *585*, 357–362.

85. McKinney, W. (2010). Data Structures for Statistical Computing in Python. In Proceedings of the 9th Python in Science Conference, S. van der Walt and J. Millman, eds., pp. 56–61.

86. Pedregosa, F., Varoquaux, G., Gramfort, A., Michel, V., Thirion, B., Grisel, O., Blondel, M., Prettenhofer, P., Weiss, R., Dubourg, V., et al. (2011). Scikit-learn: Machine Learning in Python. J. Mach. Learn. Res. *12*, 2825–2830.

87. Virtanen, P., Gommers, R., Oliphant, T.E., Haberland, M., Reddy, T., Cournapeau, D., Burovski, E., Peterson, P., Weckesser, W., Bright, J., et al.; SciPy 1.0 Contributors (2020). SciPy 1.0: fundamental algorithms for scientific computing in Python. Nat. Methods *17*, 261–272.

88. Hrvatin, S., Sun, S., Wilcox, O.F., Yao, H., Lavin-Peter, A.J., Cicconet, M., Assad, E.G., Palmer, M.E., Aronson, S., Banks, A.S., et al. (2020). Neurons that regulate mouse torpor. Nature *583*, 115–121.

89. Jain, A.K., and Farrokhnia, F. (1991). Unsupervised texture segmentation using Gabor filters. Pattern Recogn. *24*, 1167–1186.

90. Wong, T.-T. (2015). Performance evaluation of classification algorithms by k-fold and leave-one-out cross validation. Pattern Recogn. *48*, 2839–2846.

91. Huber, P.J., and Ronchetti, E.M. (2009). Robust Statistics, Concomitant scale estimates. In Robust Statistics, second edition edition (John Wiley & Sons).

92. Zhang, B., Kirov, S., and Snoddy, J. (2005). WebGestalt: an integrated system for exploring gene sets in various biological contexts. Nucleic Acids Res. *33*, W741–W748.

93. Waskom, M. (2021). seaborn: statistical data visualization. J. Open Source Softw. *6*, 3021.

94. Hunter, J.D. (2007). Matplotlib: A 2D Graphics Environment. Comput. Sci. Eng. *9*, 90–95.

95. Claudi, F., Tyson, A.L., Petrucco, L., Margrie, T.W., Portugues, R., and Branco, T. (2021). Visualizing anatomically registered data with brainrender. Elife *10*, e65751.

96. Claudi, F., and Petrucco, L. (2022). brainglobe/bg-heatmaps. https://doi.org/10.5281/zenodo.5887586.

STAR★METHODS

KEY RESOURCES TABLE

REAGENT or RESOURCE	SOURCE	IDENTIFIER
Antibodies		
anti-parvalbumin antibody	Synaptic System	Cat#195004; RRID: AB_2156476
anti-Guinea Pig IgG Alexa Fluor™ 488	Invitrogen	Cat#A11073; RRID: AB_2534117
Chemicals, peptides, and recombinant proteins		
biotinylated Wisteria Floribunda Lectin (WFA)	Vector Laboratories	Cat#B-1355-2
Streptavidin, Alexa Fluor™ 555 conjugate	Thermo Fisher	Cat#S21381
Deposited data		
Raw microscopy dataset	This study	Zenodo: https://doi.org/10.5281/zenodo.7419282
Prediction images	This study	Zenodo: https://doi.org/10.5281/zenodo.7886214
Experimental models: Organisms/strains		
Mouse: C57BL/67	Jackson Laboratory	RRID:IMSR_JAX:000664
Software and algorithms		
Zen blue software	Zeiss	RRID:SCR_013672
QuickNII v2.2	Puchades et al.[82]	RRID:SCR_016854
Visualign v0.9	NITRC	RRID: SCR_017978
MATLAB software R2021b	Mathworks	RRID:SCR_001622
Python 3.8.0	Python	RRID:SCR_008394
NumPy 1.23.5	Harris et al.[84]	RRID:SCR_008633
Pandas 1.5.2	McKinney[85]	RRID:SCR_018214
Scikit-learn 1.1.3	Pedregosa et al.[86]	RRID:SCR_002577
SciPy 1.9.3	Virtanen et al.[87]	RRID:SCR_008058
Python code for automated cell counting	Ciampi et al.[34]	Zenodo: https://doi.org/10.5281/zenodo.7985842
Python code for data analysis	This study	Zenodo https://doi.org/10.5281/zenodo.7991607

RESOURCE AVAILABILITY

Lead contact

Further information and requests for resources and reagents should be directed to and will be fulfilled by the lead contact, Tommaso Pizzorusso (tommaso.pizzorusso@sns.it).

Materials availability

This study did not generate new unique reagents.

Data and code availability

- Raw microscopy data and prediction images have been deposited at Zenodo (https://doi.org/10.5281/zenodo.7419282; https://doi.org/10.5281/zenodo.7886214)[60,61] and are publicly available as of the date of publication. DOIs are listed in the key resources table.
- All original analysis code to reproduce all figures and the original code to run the deep learning models for cell counting is available on GitHub (https://github.com/LeonardoLupori/wholeBrain_PNN_analysis, https://github.com/ciampluca/counting_perineuronal_nets), has been deposited at Zenodo[78,79] and is publicly available as of the date of publication. DOIs are listed in the key resources table.
- Any additional information required to reanalyze the data reported in this paper is available from the lead contact upon request.

EXPERIMENTAL MODEL AND SUBJECT DETAILS

Animals

All experiments were carried out in accordance with the European Directives (2010/63/EU), and were approved by the Italian Ministry of Health (authorization number 723/ 2020 PR). A total of 7 adult C57BL/6J (RRID:IMSR_JAX:000664) mice, 3 males (mouseID: CC3A, CC4A, CC4B) and 4 females (mouseID: AL1A, CC1A, CC1B, CC2B), at approximately postnatal day (P)150 were used in this study. Female animals were not sacrificed at a specific phase of their estrous cycle. Weaning was performed at P21–23. Animals were maintained at 22°C with a standard 12-h light-dark cycle. No running wheels were present in the cage. During the light phase, a constant illumination below 40 lux from fluorescent lamps was provided. Mice were housed in conventional cages (365 x 207 x 140 mm, 2-3 animals per cage) with nesting material, and had access to food and water ad libitum. During the first 12-14 weeks of life, mice were fed a standard diet (standard diet Mucedola 4RF25). Then, animals were fed a balanced purified diet (Research Diets, Inc., New Brunswick, NJ, USA, cat. no. D12450Ji) for 6 weeks before the sacrifice.

METHOD DETAILS

Immunofluorescence staining

Mice were anesthetized with chloral hydrate (20 ml/Kg BW) and perfused via intracardiac infusion with cold PBS and then 4% paraformaldehyde (PFA, w/vol, dissolved in 0.1 M phosphate buffer, pH 7.4). All perfusions were carried out between 10:00 and 12:00. Brains were extracted and post-fixed overnight in PFA 4% at 4 °C, then transferred to a 30% (w/vol) sucrose solution for 48 hours. For each brain, 50 μm coronal sections, spanning from the main olfactory bulbs (MOB) to the cerebellum (CB), were cut on a freezing microtome (Leica). One out of every 3 sections was collected for further processing, leading to a sampling of one slice every 150 μm. For a small subset of sections that did not match our quality standards due to deformations during the cutting process (on average 3.7±0.5 slices per animal), an adjacent section was collected instead. For each animal, slices were assigned a unique ID and pooled in 9-10 wells of a 24-well plate for free-floating staining. Each well contained 5-6 sections that sampled the brain at equally spaced points in the anterior-posterior axis.

Slices were blocked for 2h at room temperature (RT) in a solution containing 3% bovine serum albumin (BSA, A7906 Sigma-Aldrich) in PBS. Then, slices were incubated overnight at 4 °C with a solution containing biotinylated Wisteria floribunda Lectin (WFA, B-1355-2, Vector Laboratories, 1:200) and 3% BSA in PBS. On the following day, sections were rinsed 3 times in PBS (10 min each) at RT, incubated with a solution of red fluorescent streptavidin (Streptavidin, Alexa Fluor™ 555 conjugate, S21381, Thermo Fisher, 1:400) and 3% BSA in PBS for 2h at RT, and rinsed again 3 times in PBS. On the same day, slices were incubated with a blocking solution for parvalbumin staining containing 10% BSA and 0.3% Triton in PBS for 30 minutes, then washed 3 times (10min each) and finally incubated overnight at 4°C with primary antibody solution containing anti-parvalbumin (Parvalbumin antibody, 195004, Synaptic System 1:1000, RRID: AB_2156476) 1% BSA and 0.1% Triton in PBS. Then, sections were rinsed 3 times (10 min each) in PBS; incubated with a secondary antibody solution containing secondary antibody (anti-Guinea Pig IgG Alexa Fluor™ 488, A11073, Invitrogen, 1:500, RRID: AB_2534117), 1% BSA. plus 0.1% Triton for 2h at RT, and washed again 3 times in PBS. Finally, sections were mounted on microscopy slides with a mounting medium (VECTASHIELD® antifade mounting medium, H-100, Vector Laboratories), and stored at 4°C. All sections in each staining well were mounted on the same slide.

Image acquisition

All images were acquired using the acquisition software ZEN blue (RRID:SCR_013672) with a Zeiss Apotome.2 microscope and a 10x objective and digitized by an AxioCam MR R3 12-bit camera, resulting in a pixel size of 0.645 μm. For the WFA channel, excitation light passed through a 538-562 nm bandpass filter and a 570 nm dichroic mirror, while emitted light was filtered with a 570-640 nm bandpass filter. For the PV channel, filters were a 450-490 nm bandpass for excitation, a 495 nm dichroic mirror, and a 500-550 nm bandpass for emission. All images were acquired with the same intensity of excitation light and with an exposure time of 80 ms for the WFA channel and 850 ms for the PV channel. For all sections, we acquired 3 apotome images for optical sectioning. Each brain slice was acquired as a tiled multi-image experiment on a single z-plane selected at the depth of maximal staining intensity, typically on the side of the brain slice in direct contact with the microscope slide.

Coronal sections of the entire mouse brain span a relatively large area and even small irregularities in the microscope slide can lead to artifacts in image intensity due to the tissue section not sitting exactly perpendicular to the optical path. To account for this, we acquired each slice with a tilted z-plane linearly interpolated between 4 manually selected focus points at the edges of each section. After the acquisition, multi-image tiles were stitched in ZEN and exported as 8-bit TIFF files for further processing. The resulting dataset consisted of 842 single channel, 8-bit, TIFF images ranging from 7 to 165 MB in size and from 2646 to 17631 px (width) in resolution.

Image registration to the Allen Brain Atlas CCFv3-2017

Image preprocessing

For each mouse, all the images were ordered along the anterior-posterior axis according to their unique ID in either the anterior-to-posterior or the posterior-to-anterior direction. Images were manually inspected and, based on irregularities in the fixed brain and

anatomical landmarks, a minority of them were mirrored vertically to make sure matching hemispheres were always on the same side for the whole image sequence.

All the following steps of preprocessing and image registration were carried out on a downsampled (20% of the original size) TIFF dataset. For each downsampled experimental image, we created a matching binary mask of the same size, encoding whether each pixel belongs to brain tissue or not. Masks were automatically generated for the entire subsampled dataset by using a machine learning model (random decision forest) interactively trained with Ilastik[80] on a subset of 57 image crops (width ranging from 344 px to 526 px). Masks were used in the quantification steps to restrict fluorescence analysis only to portions of the images that contained biological tissue. All the masks were visually inspected through a custom MATLAB graphical user interface (GUI) and, if necessary, manually adjusted to correct for misclassification of small areas or to exclude parts of the tissue containing experimental artifacts from further analysis.

Image registration

We aligned our dataset to the Allen Mouse Brain Common Coordinate Framework (CCFv3-2017)[81] with a multi-step workflow: first, we used the software QuickNII v2.2 (RRID:SCR_016854)[82] to interactively assign each experimental image to a specific plane in the reference atlas based on anatomical landmarks. The software allows the selection of an arbitrary 2D plane out of the CCFv3 volume, thus improving accuracy for samples where sections were not cut on a perfectly coronal plane, but with a slight angle. In the same software, we also performed rigid transformations (i.e., rotations and translations) and uniform horizontal or vertical stretch in order to match the reference plane to each experimental image. In a second step, we used the software VisuAlign v0.9 (RRID: SCR_017978, VisuAlign) to manually apply local, non-rigid transformations to the planes selected in QuickNII in order to match the experimental images.

We then used a custom set of MATLAB functions to load the output file from VisuAlign and to generate a displacement field for each experimental image. Each displacement field defines the local non-rigid transformation as a couple of values (D_x, D_y) for each pixel, defining the displacement in the image on the X and Y axes. By using the coordinates of the 2D plane defined in QuickNII and the local transformations defined in the displacement field it is possible to match each pixel position in our experimental images (X_e, Y_e) to a voxel position in the reference atlas (X_a, Y_a, Z_a).

Deep learning models for cell counting

The deep learning models used in this work are based on a published counting strategy[34] specifically designed to account for the variability between experimenters when counting non-trivial, overlapping, or low-contrast objects like PNNs in histological preparations. Briefly, cell counting for both PNNs and PV cells was done through a two-step pipeline. In the first step, we performed cell detection by using the Faster-RCNN network[83] with a Feature Pyramid Network module and a ResNet-50 backbone. The goal of this stage is to produce a collection of putative object locations with high recall. The training dataset of this network is large but labeled by a single rater, thus it is assumed to be ''weakly labeled'', i.e., it may contain spurious (false positives) and missing annotations (false negatives). In the second step, we scored each detected object to assign it an ''objectness'' value designed to maximize its correlation with the raters' agreement. To do this, we trained a small convolutional network to rank samples with increasing agreement values and produce an increasing score for objects with increasing raters' agreement (Figures S1B and S1C). In this stage, we employed a smaller training dataset labeled by multiple raters for which the agreement between experimenters on each object was computed (see Training Datasets below).

Following this strategy, we employed four different models: a localization model for PNNs and PV cells, and a scoring model for PNNs and PV cells. From now on, we will refer to these models respectively as PNN_{loc}, PV_{loc}, PNN_{score}, and PV_{score}. We first localized and scored PNNs using PNN_{loc} and PNN_{score} and PV cells using PV_{loc} and PV_{score} on separate image channels. Then, we removed PNNs with a score lower than 0.4 and PV cells with a score lower than 0.55.

As a performance metric for this counting pipeline, we computed the mean absolute relative error (MARE) as follows:

$$\mathrm{MARE} = \frac{\sum_{n=1}^{N} \left| C_{gt}^{n} - C_{pred}^{n} \right|}{\sum_{n=1}^{N} C_{gt}^{n}}$$

where N is the number of test images, and C_{gt}^{n} and C_{pred}^{n} are the ground-truth and the predicted count of the n-th image, respectively. On the test split of our multi-rater dataset, our counting approach achieves a MARE of 0.048 and 0.080 respectively for PNNs and PV cells when considering samples located by at least 3 raters. As a final quality check, we visually inspected all the images and manually removed cases of artefactual cell detection. The source code for training models or making predictions with a pre-trained model can be found at this link.

Training Datasets

Here we describe the training dataset used for each model.

The dataset used for the PNN_{loc} model consists of 580 8-bit grayscale TIFF images (width ranging from 2646 to 17631 px) dot-annotated with the (x,y) position of each PNN for a total of 678556 PNNs. The dataset used for the PV_{loc} model consists of 53 8-bit grayscale TIFF images (width ranging from 5157 to 16389 px) dot-annotated with the (x,y) position of each cell for a total of 101348 PV cells. PNNs were annotated by looking for distinctive circular patterns of WFA staining around cell somata and proximal dendrites.

Finer PNN-like structures exclusively present in the neuropil, like those found in the olfactory bulbs,[64] were not annotated in our training dataset due to the magnification factor in our images not allowing for consistent detection of such structures.

The datasets used for the two scoring models both consist of a collection of 25 8-bit grayscale TIFF images (2000 x 2000 px). Seven expert experimenters independently dot-annotated each image for a total of 4727 PNNs and 5833 PV cells that vary in the agreement between raters from 1/7 to 7/7. Pre-trained models, ready for making predictions on new images, are available at this link.

Brain structure sets

Throughout the paper we aggregated data in three sets of brain structures differing by their level of spatial resolution or granularity. The first structure set (`structure_set_id`: 687527670) has a low level of resolution and is composed of 12 coarse-ontology major brain divisions (see Table S3). The second structure set (`structure_set_id`: 167587189) has a medium level of resolution (e.g., it comprises distinct cortical areas) and is composed of 316 mid-ontology brain regions (see Table S3).

These two structure sets were defined by the Allen Institute in their API and can be accessed using the `StructureTree` object. Lastly, for the analysis of cortical layers, we maintained the finest level of resolution present in the CCFv3-2017, where individual cortical layers are segmented (see Table S3 for the definition of cortical areas). Please note that, for the visualizations in Figures 5A and 5B, we included the lateral and medial parts of the entorhinal cortex (ENTl and ENTm, that actually belong to the hippocampal formation) given their layered structure. For all the analyses in the paper, we dropped data of any structure belonging to, or descending from the fiber tracts (`areaID`:1009) and the ventricular system (`areaID`:73).

QUANTIFICATION AND STATISTICAL ANALYSIS

All data analysis was done using custom software written in MATLAB 2021b (RRID:SCR_001622) and Python (3.8, RRID:SCR_008394). We used the following additional Python libraries for data analysis: NumPy (1.23.5, RRID:SCR_008633),[84] Pandas (1.5.2, RRID:SCR_018214),[85] Scikit-learn (1.1.3, RRID:SCR_002577)[86] and SciPy (1.9.3, RRID:SCR_008058).[87] The description of all the statistical comparisons are listed in Tables S1 and S2. The results of correlation and overrepresentation analyses, and the definition of center and dispersion measures are reported in figure legends.

Measurement of single-cell staining intensity

Quantification of the staining intensity of individual cells (PNNs or PV cells) was performed on 80x80 pixels image tiles centered on the (x,y) center positions of each PNN/cell. Within each tile, we segmented pixels belonging to the cell or the background, and the intensity of each PNN/cell was defined as the average value of the pixels belonging to that cell. The segmentation was performed by using a random forest pixel classifier implemented with the MATLAB `Treebagger` class with the support of additional custom MATLAB functions from the literature.[88] This approach allows the classification of single pixels as background or foreground, based on a collection of features of that pixel. Classifying all the pixels in an image tile results in a binary segmentation mask.

The features considered for pixel classification were the contrast-adjusted pixel intensity (using the `imadjust` MATLAB function), the position of the pixel relative to the center of the tile in the horizontal and vertical axes, and the pixel intensity in 16 versions of the image tile filtered with 16 Gabor filters. The wavelength and orientation of each Gabor represented one of the possible combinations of four different wavelength values (2.8, 5.6, 11.3, 22.6 pixels/cycle) and four different orientations (0°, 45°, 90°, 135°). Wavelengths were sampled in increasing powers of 2 starting from $\frac{4}{\sqrt{2}}$ up to the hypotenuse length of the input image tile, while orientations were sampled from 0° to 135° with a step of 45°.[89] Each random forest model for segmentation of PNNs and PV cells was trained on 69600 pixels from 1160 tiles (60 pixels randomly chosen for each tile).

Staining metrics definitions

We defined four metrics to quantitatively analyze the staining for PNNs and PV cells.

First, *diffuse fluorescence* represents the amount of average fluorescence signal in a brain region. It is defined as the average intensity of all the pixels belonging to that region across all the slices of each mouse. These values were then normalized within each mouse by dividing them by the mean pixel intensity of all the brain. This normalization removes global differences in intensity between mice (due to for example perfusion quality and post-fixation) while highlighting how staining intensity is differentially distributed across brain regions. As a result, a region with diffuse fluorescence of 1 would have a staining intensity equal to the brain average.

Second, *density* represents the number of cells or PNNs per unit of area in a brain region. It was defined as the total number of cells or PNNs belonging to that region across all the slices of each mouse, divided by the total area belonging to that region in mm^2.

Third, cell *intensity* represents the staining intensity of cells or PNNs in a brain region. Each cell was assigned a value of staining intensity (see section Measurement of single-cell staining intensity). For each region, cell intensity was defined as the average intensity of all the cells belonging to that region. These values were then normalized to the range 0–1 by dividing by 255 (maximum intensity value for 8-bit images).

Last, we defined a combined, more abstract metric, that takes into account both the number and the intensity of cells/PNNs, called *energy*. Cell energy can be thought of as a measure of cell density, weighted on intensity meaning that in the calculation of density, the weight of each cell/PNN is a value between 0 and 1 that depends on its intensity. For a region of area A, containing c cells:

$$\text{Energy} = \frac{\sum_{i=1}^{c} 1 \times intensity_i}{A}$$

These values were then normalized within each mouse by dividing them by energy calculated on the entire brain. As a result, a region with an energy value of 1 would be equal to the brain's average energy. This definition of energy is analogous to the one used by the Allen Institute[38] for the analysis of in-situ hybridization data (see the technical paper on the informatics data processing here). It is important to note that the brain of each mouse in this study has been sampled in its entire anterior-posterior axis with the same sampling rate (1 every 3 slices) thus ensuring that the normalization step for diffuse fluorescence and energy measurements does not introduce biases due to differential sampling of areas with extreme staining intensity values.

Colocalization PNN-PV

PV cells and PNNs were counted with two distinct deep learning models on separate channels. We defined a PNN and a PV cell to be colocalized based on their (x,y) position in the original image using the following criteria. We selected one cell/PNN at a time as a reference object. For each reference object, we selected only objects in the other channel with a distance equal to or smaller than 15 pixels (9.675μm). If multiple objects satisfied this criterion, we picked the closest one as a colocalized object. Otherwise, if no objects were close enough to the reference one, we defined the reference object as non-colocalized (either a PV-negative PNN or a WFA-negative PV cell).

We computed two metrics to describe PNNs and PV colocalization: first, the percentage of PV+ PNNs, that is the fraction of PNNs that are around a PV-positive cell; second, the percentage of WFA+ PV cells, that is the fraction of PV-positive cells that are surrounded by a net. Colocalization metrics at the coarse level of resolution (see section Brain structure sets for definition) were calculated independently for each mouse and the results averaged across mice. For the same analysis at higher levels of resolution (mid-ontology in Figures 3C and S4), we adopted a different strategy. At higher resolutions, brain subdivisions are much smaller and some areas contain a limited number, or even no, of PNN or PV-cells (e.g., layer 1 of cortical areas). As a result, the percentage of colocalization can vary dramatically depending on a few, or even a single cell, thus not providing a robust measure for that area (e.g., an area with 3 PV cells can vary from 0% to 100% depending on the state of PNNs on only 3 neurons). To solve this issue, we calculated colocalization metrics on a dataset of cells pooled from all animals except one, in a manner similar to the leave-one-out cross-validation approach used in machine learning.[90] We repeated this process for all mice and considered each repetition an ''experimental unit''. We then averaged across experimental units. For the analysis of the colocalization of PNNs and PV cells (Figures 3C and S4), we included only brain regions that contained at least 3 PNN and 3 PV cells in at least 4 mice.

PV intensity classes

PV cells were divided into four intensity classes of equal width based on their cell intensity levels. The classes were defined as 1: low PV (PV intensity in the range [0, 0.25)); 2: intermediate-low PV (range [0.25, 0.5)); 3: intermediate-high PV (range [0.5, 0.75)); 4: high PV (range [0.75, 1]). The probability of being surrounded by a net was estimated by dividing the total number of PV cells in that class by the number of colocalized PV-PNN cells. This analysis was done independently for each mouse. We fit data to a first-degree linear equation by using the numpy function `np.polyfit`. The estimated first- and zero-order parameters are displayed in the text insets for each plot.

Correlation between staining metrics

The analysis of correlations between staining metrics in all the figures (Figures 2E, 3D–3G, and S3E) was done by computing the Spearman's rank correlation coefficient using the SciPy function `stats.spearmanr`. In each graph, we reported the value of the correlation coefficient (r_s) and the associated p-value. We highlighted in red significant ($p < 0.05$) correlations. For significantly correlated metrics we also reported in blue a linear fit obtained using a Huber regressor robust to outliers[91] using the implementation in `sklearn.linear_model.HuberRegressor`.

Correlation with thalamic afferent connectivity

To measure thalamic input strength we used connectomics data from Table S3 of Oh et al., 2014.[46] In that dataset, we selected the connections that originated from the thalamus and that terminated in sensory-related cortical regions (SSp-n, SSp-bfd, SSp-ll, SSp-m, SSp-ul, SSp-tr, SSp-un, SSs, VISal, VISam, VISl, VISp, VISpl, VISpm, VISli, VISpor, AUDd, AUDp, AUDpo, AUDv). For Figure 5I we selected only thalamic inputs originating from the sensory-motor cortex related part of the thalamus (DORsm, area ID: 864, according to the CCFv3 nomenclature, https://atlas.brain-map.org/). For Figures S7I and S7J we selected only thalamic inputs originating from the polymodal-association cortex related part of the thalamus (DORpm, `areaID`: 856). Input strength for each cortical area was measured as the sum of connection strength from all brain regions belonging to either the DORsm or the DORpm to both the ipsilateral and contralateral parts of that cortex. To uniform the scale of PNN measurements and thalamic connectivity, we z-scored each set of data. For the correlation analysis (Figure 5I), we computed Pearson's correlation coefficient and the associated p-values. To estimate connection strength in high-WFA and low-WFA region clusters (Figure 5L inset), we averaged thalamic input strength values, obtained in the same way, of all the areas in each cluster.

Correlation with gene expression and gene set overrepresentation analysis

We correlated the distribution of PNN energy, WFA diffuse fluorescence and PV energy with the pattern of expression of approximately 18,000 genes, published by the Allen Institute.[38] The Allen Institute gene expression data were accessed through the Allen Brain Atlas API. The detailed query to the Allen Institute database is reported in the figure_06_downloadGeneExprABA.ipynb notebook in the wholeBrain_PNN_analysis github repository. We also provided the preprocessed gene expression data in the same github repository (filename: ''gene_expression_ABA_energy.csv''). In this dataset, levels of expression of each gene are derived from the signal intensity of whole-brain *in situ* hybridization essays and quantified as expression energy, a metric defined in an analogous way to PNN and PV energy. For correlation analysis, both gene expression data and PNN or PV staining parameters were expressed at mid-ontology resolution (see Table S3). The five areas showing the largest standard deviation in PNN or PV staining metrics were excluded from the analysis. We computed Spearman's rank correlation coefficient between each of the 3 staining metrics and the pattern of expression of each of the genes mapped by the Allen Institute. Correction for multiple testing was performed with Benjamini-Hochberg method. For all the analyses, we considered genes with FDR-adjusted p value<0.01 (Benjamini-Hochberg method) as significantly correlated (if Spearman's correlation coefficient was positive) or anticorrelated (if Spearman's correlation coefficient was negative) with the staining metric considered.

For the genes correlated and anticorrelated with PNN energy and WFA fluorescence, we performed gene ontology analysis using WebGestalt platform.[92] Overrepresentation of gene ontology terms (biological process domain) was tested separately for the 1,000 genes most correlated (with the largest correlation coefficient) and the 1,000 genes most anticorrelated (with the most negative correlation coefficient) with each of the two metrics. The list of all the genes present in the Allen ISH dataset was used as the background for all the analyses. Overrepresented gene ontology terms were filtered to ensure a false discovery rate<0.1 (Benjamini-Hochberg method) and clustered via affinity propagation to reduce redundancy.

We then tested for overrepresentation of gene sets related to ECM biology, defined by[59] as matrisome categories, in the 200 genes most correlated with PNN energy. As for gene ontology, the entire list of genes of the Allen ISH dataset was used as the background. To assess statistical significance, we performed hypergeometric test and corrected for multiple testing using Benjamini-Hochberg method. For each matrisome category, the enrichment ratio was calculated as the number of genes observed in both the matrisome category and the 200-gene list divided by the number of genes expected assuming independence of the matrisome set and the gene list.

Data visualization

Data visualization for all the figures was done in Python (3.8). Heatmaps, bar plots, and scatterplots were created using the libraries Seaborn (0.12.1)[93] and Matplotlib (3.4.2).[94] Rendered heatmaps of coronal brain slices were done by using BrainRender[95] and bg-heatmaps.[96]